CFD analysis of transient behavior of azimuth thrusters

Suijkerbuijk, D.W.

Award date:
2013

Technical University Eindhoven

Master Thesis

CFD analysis of transient behavior of azimuth thrusters

Author:

D.W. Suijkerbuijk

Supervisors:

dr. B.P.M. van Esch, TU/e
dr. ir. N.W.H. Bulten,
Wärtsilä Netherlands B.V.

Thermo Fluids Engineering - Process Technology
Mechanical Engineering

May 2013

Report number: WPT 201321

Abstract

The existing loads on an azimuth thruster are not that straight forward, especially not for operating conditions deviating from the straight forward sailing condition. In the presented work a RANS method is used to get insight in the flow phenomena and to investigate the hydrodynamic forces acting on a thruster unit, for straight inflow conditions as well as conditions with oblique inflow. Before the numerical simulations were done, the behavior of the thruster was previously investigated in model tests, carried out by Marintek in Norway. This work consist of different loading conditions for the steerable thruster unit according to the model tests, but also extended with a whole range of ship advance speeds.

For the applied study the commercial CFD solver Starccm+ is used. Different settings were used to investigate the best way of getting good results for the performance characteristics. Validation of the numerical results is made by a comparison with the experiments data. It is seen that the moving mesh method gave a good agreement with the model tests and that this method captures the flow phenomena very well.

By use of CFD the contribution of components of a thruster unit could be studied, showing that the nozzle has a large influence on the performance characteristics. For a whole thruster unit it is observed that the performance is strongly dependent of the ship speed, but also of the angle of the thruster towards the flow. The behavior in the performance results were studied to get physical understanding of the causes of the asymmetric thrust results for negative and positive heading angles. This asymmetry could be explained by correcting the results with the effects of the pre-rotation in the flow in front of the propeller plane.

The final aim of this thesis is to study the changes in the hydrodynamic forces for an azimuth thruster with a fixed angle towards the heading directions and the addition of the actual steering action, so for constantly varying steering angles. The rotation of the unit with constant speed has an effect on the side loads of the thruster unit and therefore influences the hydrodynamic steering torque to a certain extent.

Samenvatting

De krachten uitgeoefend op een stuurbare thruster zijn niet altijd voor de hand liggend, zeker niet voor condities afwijkend van de recht vooruit varende conditie. In dit werk wordt gebruik gemaakt van een RANS methode, om inzicht te verkrijgen in het stromingsgedrag en de hydrodynamische krachten werkend op een thruster te onderzoeken, zowel voor rechte instroom condities als voor condities met schuine instroom. Alvorens de numerieke simulaties zijn uitgevoerd is het gedrag van de thruster onderzocht door middel van model testen, uitgevoerd door Marintek in Noorwegen. Dit werk bevat verschillende belasting condities voor een stuurbare thruster behorende bij de model testen, maar ook uitgebreid met een hele reeks aan schip snelheden.

Voor de toegepaste studie is gebruik gemaakt van commerciële CFD solver Starccm+. Verschillende instellingen zijn gebruikt om te onderzoeken wat de beste manier om goede resultaten te krijgen voor de prestatie karakteristieken. Validatie van de numerieke resultaten zijn gedaan door vergelijking met experimentele data. Hieruit volgde dat de moving mesh methode goede overeenkomstigheden vertoonde met de model testen en dat deze methode de stromingsfenomenen goed meeneemt.

Door het gebruik van CFD kan het aandeel van de verschillende componenten worden bekeken. Dit laat zien dat de nozzle een grote invloed heeft op de prestatie karakteristieken. Voor de gehele thruster bleek dat de prestaties sterk afhankelijk zijn van de schip snelheid, maar ook van de hoek die de thruster maakt ten opzichte van de stroming. Het gedrag van de waargenomen resultaten zijn bekeken om physisch te begrijpen wat de oorzaken zijn van de asymmetrische resultaten voor negatieve en positieve stuur hoeken. Deze asymmetrie kan worden verklaard door het deze te corrigeren door rekening te houden met de voor-oriëntatie in de stroming voor het propeller vlak.

Het laatste doel van deze thesis is de veranderingen in de hydrodynamische krachten te bekijken voor een stuurbare thruster met een vaste stuurhoek ten opzichte van de stromingsrichting en een extra toegevoegde stuurbeweging, dus voor constant veranderende stuurhoeken. De rotatie van de unit met constante snelheid heeft effect op de zijwaartse belasting op de thruster en heeft daardoor in zekere mate invloed op de hydrodynamische stuurmomenten.

Acknowledgements

This report describes a project that I have conducted at Wärtsilä Netherlands in Drunen. This thesis is written in partial fulfilment of the requirements for the degree of Master of Science in Mechanical Engineering at Eindhoven University of Technology. In this section I would like to thank several people that helped me throughout this master thesis project by giving me useful advice and critical reflection.

At Wärtsilä, I especially would like to thank Norbert Bulten for giving me the opportunity to conduct my master thesis project at Wärtsilä. He also provided me with good input and ideas for the analyses of the results. I would like to thank the rest of the CFD team as well, for their advice during my learning process within Starccm+

At Eindhoven University of Technology, I would like to thank Bart van Esch for his confidence in the progress of my thesis at Wärtsilä without that many moments of contact. Besides that I would like to thank him for his critical feedback to improve the final content of this thesis.

Contents

List of Figures

Symbols

A_0	Steering Amplitude	-
A_k	Amplitude of the blade fluctuations	-
D	Propeller diameter	m
D_{blade}	Blade drag force	N
$dFxx$	Additional side force	N
F_{sail}	Thrust in sailing direction	N
F_x	Side Force	N
$F_{x_{0deg}}$	Straight inflow side force	N
$\mathbf{g}$	Gravitational acceleration	m/s^2
J	Advance coefficient	-
J_{eff}	Effective advance coefficient	-
$J_{x\,eff}$	Effective sideward coefficient	-
L_{blade}	Blade lift force	N
k	Turbulence kinetic energy	-
K_{dF_x}	Additional side force coefficient	-
$K_{dF_x\,Dyn}$	Re-scaled additional side force coefficient	-
K_{F_x}	Side force coefficient	-
$K_{F_x\,eff}$	Effective side force coefficient	-
$K_{\dot{m}}$	Mass flow coefficient	-
$K_{\dot{m}\,eff}$	Effective mass flow coefficient	-
K_{M_y}	Steering torque coefficient	-
$K_{M_y\,eff}$	Effective steering torque coefficient	-
$K_{M_{zx}}$	Thrust eccentricity coefficient	-
$K_{M_{zx}\,eff}$	Effective thrust eccentricity coefficient	-
$K_{M_{xz}}$	Side force moment coefficient	-
$K_{M_{xz}\,eff}$	Effective side force moment coefficient	-
K_T	Thrust coefficient	-
$K_{T\,eff}$	Effective thrust coefficient	-
K_{T_p}	Propeller thrust coefficient	-
$K_{Q\,eff}$	Effective propeller torque coefficient	-
$\dot{m}$	Mass flow	kg/s
M_y	Steering torque	Nm
$M_{y_{0deg}}$	Straight inflow steering torque	N
n	Rotational speed	rps
n_{eff}	Effective rotational speed	rps

r	Radius to the propeller axis	m
r_x	Thrust eccentricity	m
r_z	Arm of the side force	m
$r_{z_{0deg}}$	Straight inflow arm of the side force	m
R	Propeller radius	m
Re	Reynolds number	-
T	Propeller thrust	N
T_{blade}	Propeller blade thrust	N
Q	Propeller torque	Nm
Q_{blade}	Propeller blade torque	Nm
$\mathbf{v}$	Velocity vector	m/s
$\vec{V}$	Velocity vector	m/s
v_{tip}	Velocity at the propeller tip	m/s
V_a	Speed of advance	m/s
V_z	Axial velocity	m/s
V_t	Tangential velocity	m/s
$\vec{W}$	Relative velocity vector	m/s
α	Angle of incidence	deg
δ	Heading angle	deg
ϵ	Turbulence dissipation	-
ω_0	Blade Frequency	Hz
ω	Angular frequency	rad/s
ρ	Fluid density	kg/m^3
η_0	Efficiency	-
η_{0eff}	Effective efficiency	-
μ	Dynamic viscosity	Pa/s
μ_T	Turbulent viscosity	kg/ms
ϕ	Inflow angle	deg
ϕ_k	Phase shift	
θ	Blade angle	deg
Ω	Steering rotation rate	rps

Chapter 1

Introduction

Offshore vessels, drilling rigs, cruise ships, and ferries are often equipped with steerable thrusters. One of the main goals of these thrusters is to have the ability to deliver thrust in all directions and therefore improve their maneuverability. Their steering performance is a real advantage, especially at zero speed, where rudders are ineffective in the absence of forward velocity. Also a better accuracy of dynamic positioning and effective braking are performance related improvements [12][9]. Another additional benefit of the steerable thrusters is an increase of cargo volume, by saving machinery space. By using an electrically driven thruster, the inboard machinery installation does not have to be placed directly in front of the propellers, which gives the designers a lot more flexibility for the placement of the machinery components [4].

Hydrodynamic loads on the external components of the steerable thruster are important for the design of bearings, bevel gears and seals, and other mechanical components. Due to steering, the thruster operates at non-zero inflow angles. Hydrodynamic loads, such as the thrust eccentricity moment and the side force moment will become significant. Therefore, additional care should be taken for designing these components, considering the hydrodynamic loads. Hence, to get insight in the loads acting on these parts while steering, special knowledge is required. This information is essential for reasonable strength predictions.

A numerical method such as CFD, could provide the essential knowledge of the physical phenomena and the flow patterns that occur due to oblique inflow. An interesting advantage of using CFD above experiments for the analysis of the behavior of a thruster is that numerical methods are very well suited to analyse the different components of a thruster unit. For accurate results a detailed numerical method is necessary. To assess whether this method is realistic and reliable, the numerical results will be compared with model scale measurements. With the use of a appropriate CFD model, it also makes it possible to extend and vary the operating conditions in a short amount of time.

This master thesis consists of recent work completed at Wärtsilä. It documents the research of the quasi-steady and unsteady maneuvering forces associated with steerable thrusters, and provides insight towards the maneuvering attributes and performance. The aim of this master thesis is to present a basic understanding and quantify the quasi-steady and dynamic effects associated with steerable thrusters.

1.1 Main Thruster Parts

A steerable thruster consists of the following main components: a steering and an upper gearbox, a hydraulic system, a remote control system and a diesel or electric drive motor system [4], shown in red in Figure 1.1. These components are all needed to generate the thrust which is required for maneuvering and positioning the vessel. The generated thrust and the incoming current results in forces, which do not act on the inner parts of the thruster, but at the outside, the thruster body including propeller. The different parts considered in this thesis are the propeller, the nozzle, the pod, the shank, and the top and bottom connection (brackets), shown in black in Figure 1.1.

1.2 Definition of Forces

An impression of thruster propulsion can be obtained by considering the forces and moments that result from the thruster parts operating at an oblique angle to the incoming flow. These forces and moment are acting on the vertical axis of the thruster, with the exception of the propeller torque. To visualize this, an intersection of the thruster unit in a negative heading direction is made (Figure 1.2). First the hydrodynamic thrust

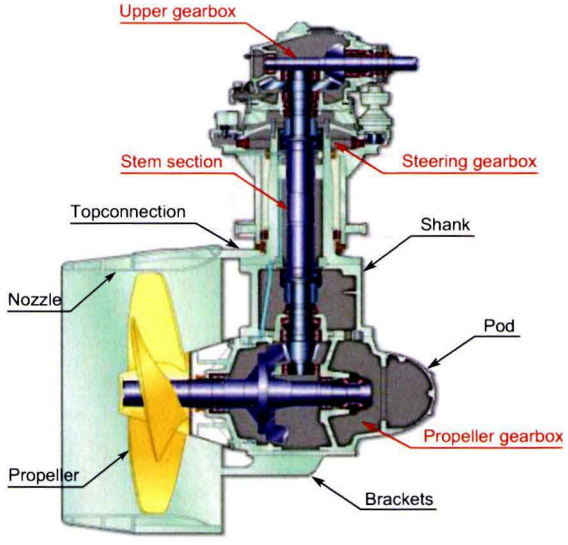

FIGURE 1.1: Main thruster parts.

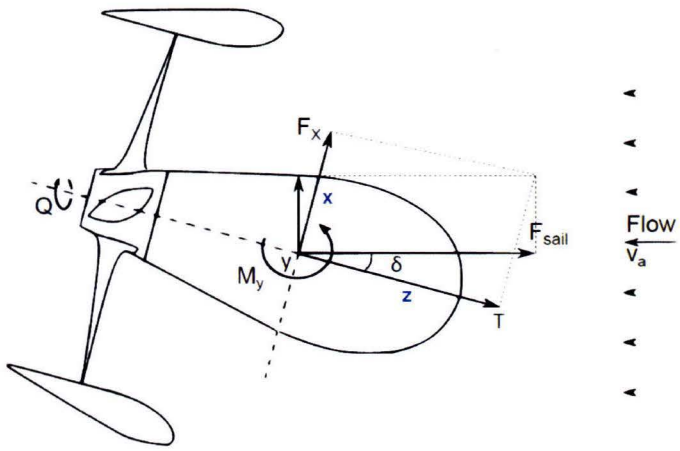

FIGURE 1.2: Definition of forces.

force and propeller torque in z-direction are symbolized by T and Q. The z-direction is the axis along the propeller shaft. The thrust components represent the net forces on the thruster unit, so also drag forces on the unit are taken into account. The heading direction is given by the heading angle δ, which leads to the thrust in the heading direction F_{sail}. This force is always in alignment with the flow direction. The thruster heading angle δ is negative if the thruster is turned in clockwise direction and positive if it is turned in anti clockwise direction, when viewed from above. In de x-direction, perpendicular to the thrust, the side forces are acting, represented by F_x. It should be noted that for azimuth thrusters, a hydrodynamic steering moment M_y exists about the y-axis, the steering shaft.
To get knowledge of the behavior of each different part of the thruster, each individual part will be separately analyzed. This method makes it possible to see the contribution of each part. Therefore, referring to forces and moments of the individual parts of the thruster unit, are referred to using appropriate subscripts, as will be seen in section 4.2.

1.3 Thruster Performance Characteristics

For discussion purposes, performance characteristics of a thruster are represented by basic open water parameters. These relate to the description of the forces and moments acting on the thruster components when operating in a uniform fluid stream. It is common within marine propulsion to express these forces and moments in terms of a series of non-dimensional characteristics [2]. The general performance characteristics

can be expressed in non-dimensional terms as follows:

$$\text{Advance coefficient} \quad J = \frac{V_a}{nD}$$

$$\text{Thrust coefficient} \quad K_T = \frac{T}{\rho n^2 D^4}$$

$$\text{Torque coefficient} \quad K_Q = \frac{Q}{\rho n^2 D^5}$$

$$\text{Efficiency} \quad \eta_0 = \frac{J}{2\pi}\frac{K_T}{K_Q}$$

Where:

V_a is the advance speed [m/s]
n is the rotational speed [rps]
D is the propeller diameter [m]
T is the thrust [N]
Q is the propeller torque [Nm]
ρ is the mass density of the fluid [kg/m^3]

For general thruster or propeller calculations for straight inflow conditions these are the characteristics used. Looking at thrusters with oblique inflow the hydrodynamic steering moment will become important. The equation to determine the steering moment consists of two different components:

$$M_y = M_{zx} + M_{xz} = T \cdot r_x + F_x \cdot r_z \tag{1.1}$$

Therefore the performance characteristics could be extended with the following terms:

$$\text{Side force coefficient} \quad K_{F_x} = \frac{F_x}{\rho n^2 D^4}$$

$$\text{Steering moment coefficient} \quad K_{M_y} = \frac{M_y}{\rho n^2 D^5}$$

$$\text{Thrust eccentricity moment coefficient} \quad K_{M_{zx}} = \frac{T r_x}{\rho n^2 D^5}$$

$$\text{Side force moment coefficient} \quad K_{M_{xz}} = \frac{F_x r_z}{\rho n^2 D^5}$$

Where:

F_x is the force in normal direction [N]
M_y is the steering moment around the vertical axis [Nm]
r_x is the thrust eccentricity [m]
r_z is the length of the lever-arm of the side force [m]

The underlying phenomena of the steering moment and associated components, the thrust eccentricity M_{zx} and the side force moment M_{xz} will be discussed in more detail in section 4.1.

Chapter 2

Numerical Approach

The Navier-Stokes equation describes the dynamic behavior of fluid motions by a set of coupled partial differential equations. This Navier-Stokes equation needs to be solved to investigate the dynamical flow effects acting on the thruster. Since an analytical solution cannot be found for complex geometries like a thruster, the equations need the be solved by a Computational Fluid Dynamics code (CFD), making use of a finite volume method. For this thesis, the commercial solver Starccm+ version 7.04, is used.

Discussions of the application of the numerical method are divided into three parts, (i) the selection of the computational domain, (ii) discretizing the computational domain into finite elements and (iii) the selection of the boundary conditions.

2.1 Governing Equations

2.1.1 Conservation Laws

The flow through a thruster can be approximated as an isothermal process in which the temperature remains constant. To describe such a flow problem, two conservation laws apply. At first the principle of mass conservation (equation 2.1) [5], which describes that the time rate of change of mass in a control volume is balanced with the flux of the mass across the control volume surface:

$$\frac{\partial \rho}{\partial t} + \nabla \cdot (\rho \mathbf{v}) = 0 \tag{2.1}$$

with ρ the density of the fluid and $\mathbf{v}$ the velocity vector. Secondly the conservation of momentum [5], also known as the Navier-Stokes equations, given by:

$$\rho \left(\frac{\partial \mathbf{v}}{\partial t} + \mathbf{v} \cdot \nabla \mathbf{v} \right) = -\nabla p + \mu \nabla^2 \mathbf{v} + \frac{1}{3} \mu \nabla (\nabla \cdot \mathbf{v}) + \rho \mathbf{g} \tag{2.2}$$

where p is the pressure, μ the dynamic viscosity of the fluid and $\mathbf{g}$ the acceleration of gravity. Assuming that the fluid is Newtonian and incompressible, equations 2.1 and 2.2

reduce to:

$$\nabla \cdot \mathbf{v} = 0 \tag{2.3}$$

$$\rho\left(\frac{\partial \mathbf{v}}{\partial t} + \mathbf{v} \cdot \nabla \mathbf{v}\right) = -\nabla p + \mu \nabla^2 \mathbf{v} + \rho \mathbf{g} \tag{2.4}$$

In principle, the Navier-Stokes equations can now be solved directly without further assumptions. For turbulent flows, this requires direct numerical simulation (DNS). For most flow problems, unfortunately, it leads to a time consuming process, because it requires a sufficiently fine mesh and a small enough time step to resolve every spatial and temporal scale of turbulence. In the next section, a method to reduce the computational effort will be discussed.

2.1.2 Introducing RANS Turbulence Model

The Reynolds-Averaged Navier-Stokes(RANS) is the oldest approach to turbulence modeling. In the RANS approach, the Navier-Stokes equations are solved for time-averaged quantities. The principle of Reynolds averaging is based on a decomposition of the variables in a time averaged value and a fluctuating part: $\mathbf{v} = \overline{v} + v'$. The turbulent flow is thus solved statistically which reduces the computational effort compared to DNS. However, the averaging procedure introduces additional terms in the equations which act as stresses in the fluid, the so-called turbulent or Reynolds stresses. Additional equations are needed to solve for the extra unknowns. This is known as the closure problem. The additional equations are also referred to as the turbulence model.
One of the closure hypothesis was proposed by Boussinesq. In this method the Reynolds stress term is defined as:

$$-\rho\overline{v_i' v_j'} = \mu_T\left(\frac{\partial \overline{v_i}}{\partial x_j} + \frac{\partial \overline{v_i}}{\partial x_i}\right) - \frac{2}{3}\rho k \delta_{ij} \tag{2.5}$$

where k refers to the turbulent kinetic energy defined as:

$$k = \frac{1}{2}\overline{v_i' v_i'} = \frac{1}{2}(\overline{v_x' v_x'} + \overline{v_y' v_y'} + \overline{v_z' v_z'}) \tag{2.6}$$

and μ_T refers to the turbulent viscosity. To determine a value for this turbulent viscosity μ_T different eddy viscosity turbulence models can be used.

2.1.3 Eddy Viscosity Turbulence Model

Each turbulence model has its own advantage or disadvantage for a particular application. Two well known models are the k-ϵ model which was first presented by Jones and Launder in 1972 and the k-ω model which was postulated by Kolmogorov. The focus in this thesis will be on the k-ϵ turbulence model.

2.1.3.1 Standard k-ϵ Model

The turbulent kinetic energy, for the standard k-ϵ model, follows from the following transport equations [11], for turbulent kinetic energy k:

$$\frac{\partial}{\partial t}(\rho k) + \frac{\partial}{\partial x_i}(\rho k v_j) = \frac{\partial}{\partial x_j}\left[\left(\mu + \frac{\mu_T}{\sigma_k}\right)\frac{\partial k}{\partial x_j}\right] + P_k + P_b - \rho\epsilon - Y_M + S_k \tag{2.7}$$

and for the rate of dissipation ϵ:

$$\frac{\partial}{\partial t}(\rho\epsilon) + \frac{\partial}{\partial x_i}(\rho\epsilon v_j) = \frac{\partial}{\partial x_j}\left[\left(\mu + \frac{\mu_T}{\sigma_\epsilon}\right)\frac{\partial \epsilon}{\partial x_j}\right] + C_{1\epsilon}\frac{\epsilon}{k}(P_k + C_{3\epsilon}P_b) - C_{2\epsilon}\rho\frac{\epsilon^2}{k} + S_\epsilon \tag{2.8}$$

With μ_T the turbulent viscosity defined as:

$$\mu_T = \rho C_\mu \frac{k^2}{\varepsilon} \tag{2.9}$$

and C_μ a constant. The terms in the above equation P_k and P_b represents the generation of the turbulence kinetic energy due to the mean velocity gradients and the turbulence kinetic energy due to buoyancy. Y_m represents the contribution of the fluctuation dilatation in the compressible turbulence to the overall dissipation rate. S_k and S_ϵ are source terms $C_{1\epsilon}$ and $C_{2\epsilon}$ and $C_{3\epsilon}$ are some constants.
The model requires two additional equations in each direction, which means that a total of 6 additional equations need solving.

2.1.3.2 Realizable k-ϵ Model

The realizable k-ϵ model differs from the standard k-ϵ model by expressing the critical coefficient of the model, C_μ as a function of mean flow and turbulence properties, instead of assuming it to be constant [3]. This allows the realizable k-ϵ model to satisfy certain mathematical constraints on the normal stresses consistent with the physics of turbulence. Therefore, this model is chosen above the standard k-ϵ model. The typical flow phenomena have to be captured well to get a proper solution. For ducted propellers these phenomena occur at the clearance between propeller tip and nozzle and the flow at the trailing edge of the blade and the nozzle. From experiences in the past, the realizable k-ϵ turbulence model in Starccm+ seems to capture the flow phenomena well and gives a good agreement with the open water characteristic for the numerical solutions and the experimental results. In section 3.3.2 will be validated whether this model captures the phenomena right in case of oblique inflow as well. A detailed explanation of the realizable k-ϵ model is shown below.

For the realizable k-ϵ model (Shin et al. 1995 [10]) the turbulence kinetic energy is exactly the same as equation 2.7, whereas the rate of dissipation can be obtained from the equation below.

$$\frac{\partial}{\partial t}(\rho\epsilon) + \frac{\partial}{\partial x_i}(\rho\epsilon v_j) = \frac{\partial}{\partial x_j}\left[\left(\mu + \frac{\mu_T}{\sigma_\epsilon}\right)\frac{\partial \epsilon}{\partial x_j}\right] + \rho C_1 S\epsilon - \rho C_2 \frac{\epsilon^2}{k + \sqrt{\nu\epsilon}} + C_{1\epsilon}\frac{\epsilon}{k}C_{3\epsilon} + P_b + S_\epsilon$$

(2.10)

Where $C_1 = \max\left[0.43, \frac{\eta}{\eta+5}\right]$, $\eta = S\frac{k}{\epsilon}$ and C_2 is constant. For the determination of the turbulence viscosity μ_T equation 2.9 can be used. Where C_μ is no longer a constant but is instead given by:

$$\mu_T = \frac{1}{A_0 + A_s U^{(*)} \frac{k}{\epsilon}} \tag{2.11}$$

where:

$$U^{(*)} = \sqrt{\mathbf{S} : \mathbf{S} - \mathbf{W} : \mathbf{W}} \tag{2.12}$$

With $\mathbf{S} = \frac{1}{2}(\nabla \mathbf{v} + \nabla \mathbf{v}^T)$ the strain rate tensor and $\mathbf{W} = \frac{1}{2}(\nabla \mathbf{v} - \nabla \mathbf{v}^T)$ the rotation rate tensor given. The coefficients are given by:

$$\begin{aligned} A_s &= \sqrt{6}\cos\phi \\ \phi &= \frac{1}{3}\arccos\sqrt{6}W) \\ W &= \frac{S_{ij}S_{jk}S_{ki}}{\sqrt{S_{ij}Sij}^3} \\ A_0 &= 4.0 \end{aligned} \tag{2.13}$$

Where S is the modulus of the mean strain rate tensor $S = \sqrt{2\mathbf{S} : \mathbf{S}}$.

2.2 CFD of the Thruster Unit

2.2.1 Computational Domain

Before numerical simulations are operable, a flow domain has to be defined around the model. This has to be modeled in a Computer Aided Design environment (CAD). Because of the jet released by the thrust of the propeller, the domain has to be large, so the jet will not be disturbed by the boundary conditions of the domain. Therefore the thruster unit is modeled within a cubic domain with a length of 48 times the propeller diameter and a depth of 8 times the propeller diameter.

In order to investigate the behavior of a thruster unit with oblique inflow, the decision is made to rotate the thruster unit instead of changing the direction of the incoming flow. No changes in boundary settings are then needed for varying heading angles. Unfortunately, rotating the thruster unit in the domain requires a new mesh to be created. This is a cumbersome process since it cannot be automated; a complex mesh like this will need considerable user-interaction to prevent the occurrence of bad cells. This is the reason why the thruster unit is placed within in a cylindrical domain. It allows the thruster unit to be rotated without the need to generate a new mesh; only the cell connections on the cylindrical interface need to be re-established. The addition is made in the usual domain, illustrated in the Figure 2.1. The whole domain is now

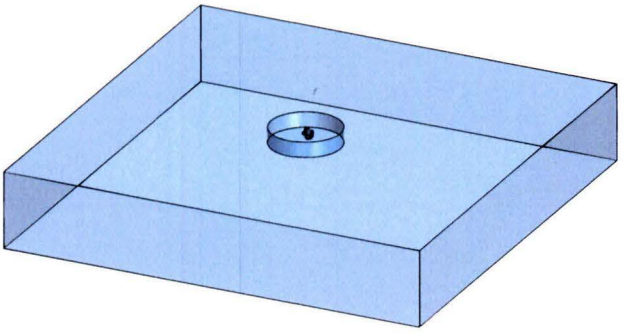

FIGURE 2.1: Fixed outer domain and the cylindrical domain.

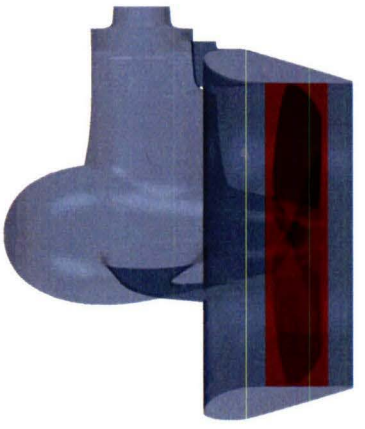

FIGURE 2.2: Rotating propeller domain.

build up into three major regions, (i) a fixed outer domain, (ii) a cylindrical domain which includes the thruster unit and (iii) the propeller domain. The essential part of a thruster to deliver thrust is the propeller. In order to have the possibility to rotate the propeller without renewing the mesh each time step, two sliding surfaces are made inside the nozzle. These intersections are made just upstream and downstream of the propeller, so that the propeller is separated from its surroundings. This propeller region at the inside of the nozzle is shown in Figure 2.2. This splits the cylindrical domain, into a fixed region of the thruster and a rotating propeller region, allowing to simulate the propeller rotation.

2.2.2 Mesh Properties

The next step in completing the model is to create a high quality mesh. The strategy is based on accurate extrusion layers near the surfaces of the thruster and the propeller. In this way the boundary layer development will be captured well. In the rest of the domain a structured hexagonal mesh is used, with volumetric refinements near the regions of interest. Figure 2.3 clearly shows the extrusion layers and the hexagonal mesh. Since the radius at the edge of the propeller is quite small, there will be a refinement around this edge, to mesh the propeller geometry within acceptable accuracy. In these areas with high gradients in the flow field, a local refinement is desirable as well. These refinements applied can be recognized well in Figure 2.4. The number of cells in a typical thruster mesh is about 3-5 million. Transient calculations with this amount of cells will cost a lot of computation time. To reduce this, the cell number has been reduced to about 1.5 million cells.

Literature suggest for the k-ϵ turbulent model y+ value, the dimensionless distance from the wall to the cell center of the first cell, between 30 and 500 are acceptable [14]. In case of the coarse mesh settings the walls y+ values are mostly within this allowed limit, ranging from 10 to 230. The effect of the cell reduction on the performance characteristics is discussed in section 3.2.

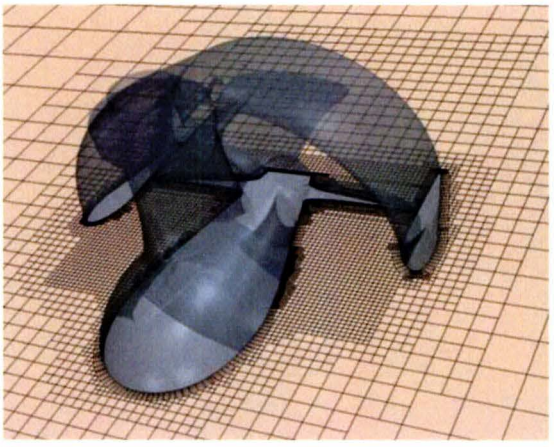

FIGURE 2.3: Thruster mesh visualization in horizontal plane.

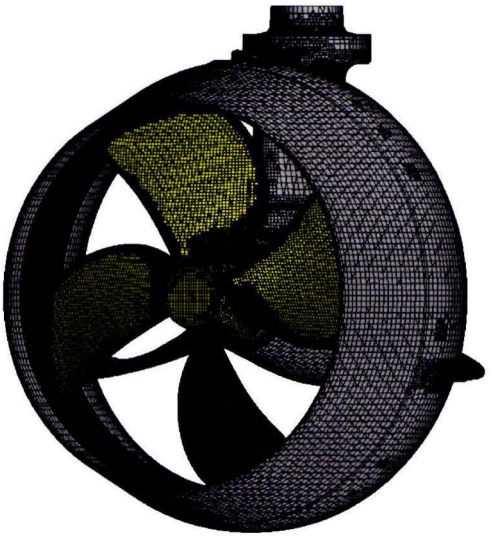

FIGURE 2.4: Refinements in the propeller mesh.

2.2.3 Boundary Conditions

After the computational domain is made and the mesh is generated, the cell faces at the boundaries need to be assigned with some type of boundary condition. At the inlet of the domain, a uniform flow is created by applying an inlet type boundary condition. Prescribing a uniform flow implies that the flow is not affected by hull of the ship. This inlet condition needs to be prescribed by a velocity in the flow direction, but also values for the turbulence intensity and the length scale require a prescription. The values are, based on experience, set to 0.5% for the intensity and 0.001 m for the turbulence length scale, which is approximately 0.4% of the propeller diameter. The top surface of the domain is prescribed as a symmetric boundary, this means that all fluxes into the boundary are zero, and there is no friction at it. At remaining surfaces of the outer domain a pressure boundary condition of 1e5 Pa is set. At the walls of the thruster unit a wall boundary condition is applied. This condition enforces a no-slip condition, which sets the normal velocity to zero and the tangential fluid velocity equal to the wall velocity. This simulates the effect of the wall on the flow. The remaining unprescribed surfaces are the intersections between the three earlier mention regions. For these surfaces a internal interface boundary setting is used. This boundary condition makes it possible to combine regions of the same type in the same continuum. These boundary conditions are good for implementing physical models like fans and propellers.

The rotating velocity can be imposed in two ways. One is to apply a moving-frame-of-reference (MRF) to the rotating propeller region. MRF is a quasi-steady approximation of the unsteady flow. The advantage of using a MRF is that there are no rotating parts, only the fluid is experiencing the behavior of a rotation propeller, by applying body forces, like centrifugal and Coriolis forces, on a particular object. Another possibility is to simulate the rotation of the propeller step by step. With this method the actual movement of the propeller is taken into account. For this fully transient calculation,

the method of moving mesh (MM) is required. For these calculations the time step was chosen equivalent to 2° of propeller rotation. This way of simulating the propeller costs a lot more computation power, but will be proven to be necessary for some cases.

The solution is based on a second order upwind differencing scheme for the momentum equation. The k-ϵ turbulence model equations are discretized with a second order upwind differencing scheme as well. Figure 2.5 shows the convergence behavior of a calculation with straight inflow for J=0.343. The first 200 steps of the 1700 steps using the MRF-method are carried out with a first order scheme, the next 1500 with a second order scheme. This converged solution is the initial condition for the MM calculations. Using the MM-method, only the first 1800 steps are again carried out with a first order scheme. For each time step a value of 10 inner iterations is being set.

2.2.4 Fluid Properties

For the thruster analysis the fluid properties for water are selected. In section 2.1.1 the flow was considered to be incompressible and Newtonian, resulting in a constant density ρ and dynamic viscosity μ. All calculations are carried out with a density of 1000 kg/m^3 and a the dynamic viscosity of 0.001 Pa/s.

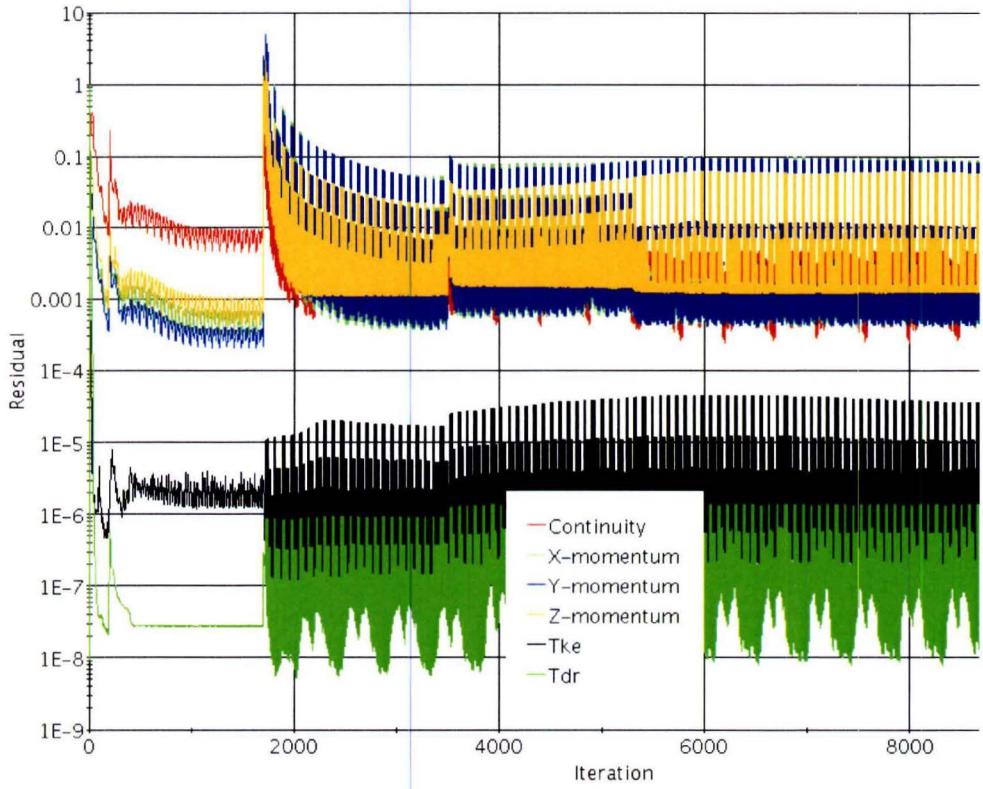

FIGURE 2.5: Convergence of a calculation with a shaft speed of 12 rps and an advance speed of 1.03 m/s, corresponding to J=0.343 (δ=0).

Chapter 3

Validation with the Experimental Results

The numerical method has been validated with the aid of experimental data. These model scale measurements have been done in an open water set-up at Marintek in Norway. This means that the performance of an isolated thruster is tested, without the interaction with the hull of the ship. In order to get a sufficiently high Reynolds number the model scale propellers are made with a diameter D of 250 mm. This should be big enough according to the Internal Towing Tank Conference, ITTC [7]. To verify this, an estimation of the Reynolds number Re is made using equation 3.1:

$$Re = \frac{\rho v_{tip} D}{\mu} \tag{3.1}$$

with ρ the density, μ the viscosity, v_{tip} the tip speed of the propeller blade. For this configuration, with a propeller rotation rate of 10.8 rps, this results in a the Reynolds number of about $2{\cdot}10^6$. Which is a lower value than the Reynolds number of about $1{\cdot}10^8$ of a full scale propeller, nevertheless it can be regarded as a sufficiently high Reynolds number.

3.1 Model Scale Test Setup

A picture of the model scale test setup with model scale thruster is shown in Figure 3.1. The propeller thrust and torque and the total unit thrust, side force and steering moment are measured. The propeller rate of revolutions is measured by a tachometer and the thruster angle is governed by a PC-controlled servo during oblique inflow test. Multiple measurements have been carried out with this thruster. At first a normal open water test is performed, without any oblique inflow. In an open water experiment the thruster is attached to a carriage and forced to move at constant speed through still water. The orientation of the thruster to the forward direction can be at an angle to simulate oblique inflow. An example of sailing at fixed oblique inflow can be found

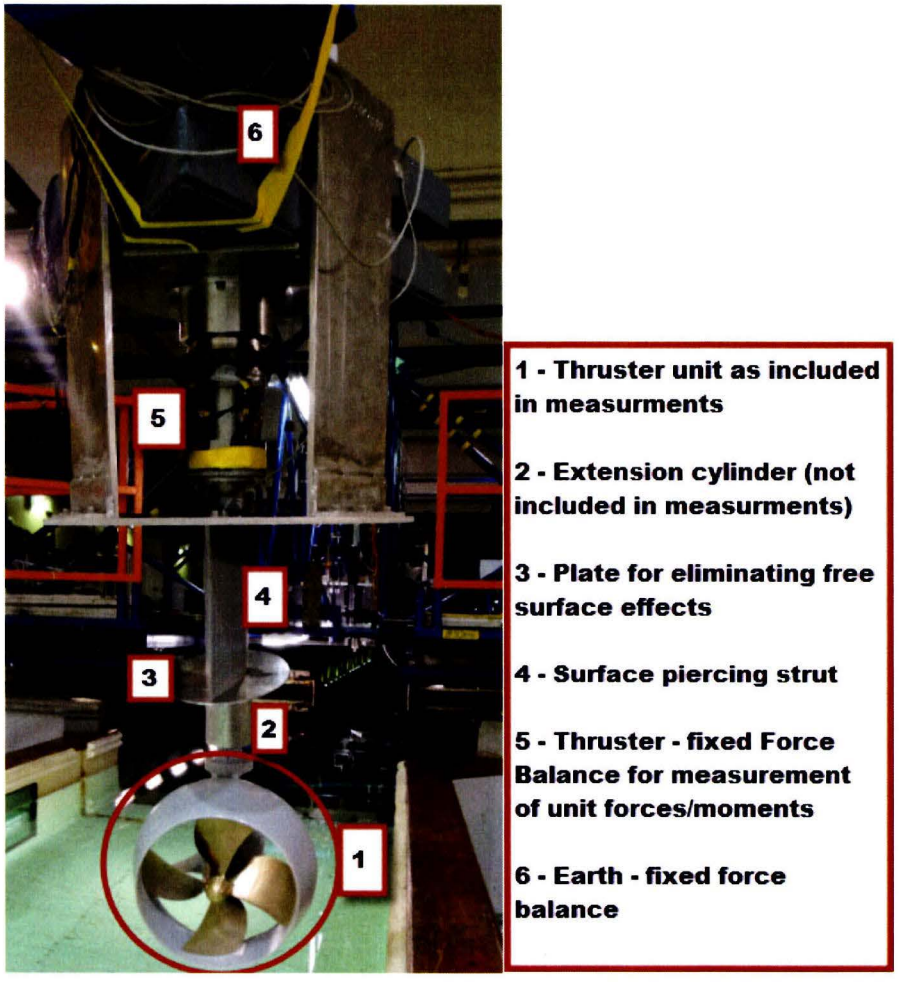

FIGURE 3.1: Model scale thruster test setup.

in OMAE 2013-10350 [8]. In practice, multiple thrusters are sometimes positioned at an oblique orientation to avoid interaction between consecutive thrusters. Interaction will always lead to degradation of total thrust, thus a degradation of the vessel speed, because of blockage of a jet by another thruster and, secondly, a reduced efficiency of a thruster due to a distorted incoming flow field [12]. These oblique inflow tests are carried out giving the thruster unit a constant forward velocity and propeller rotation, but with an azimuth angle δ with respect to the heading direction. The heading direction δ varies from -60 to 60 degrees (see Figure 1.2). In these tests the propeller thrust T_p and torque Q of the propeller are measured on the propeller shaft. At the top of the unit, the total thrust T, side force F_x and steering moment M_y are measured (see section 1.3).

3.2 Open Water Results

The open water tests are carried out for several operating conditions at an heading direction of δ=0. The measurements are done for propeller shaft speeds in the range of 10.8 to 16 rps. The advance speed V_a varies from 0 to 2.4 m/s. The performance of the

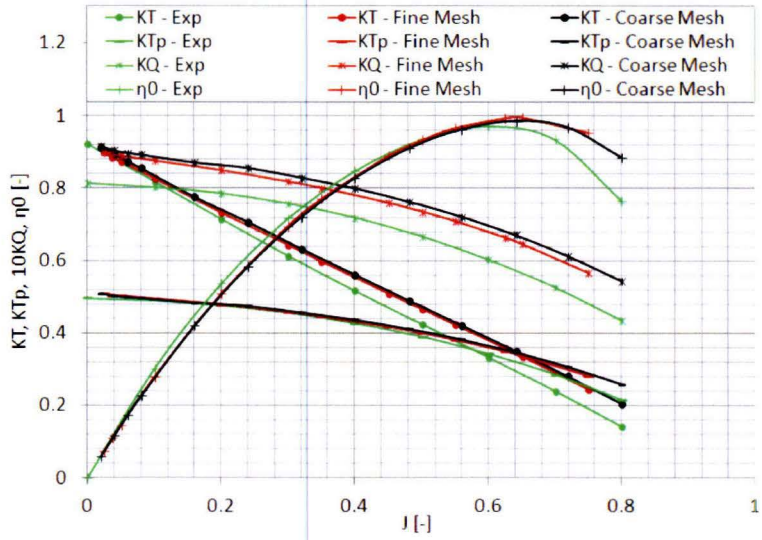

FIGURE 3.2: Comparison between model scale experiments and CFD results, for fine and coarse meshes. The results show thruster open water performance (δ=0).

thruster unit, with a shaft speed of 10.8 rps, will be represented by the dimensionless coefficients K_T, K_Q, η_0 and the propeller thrust K_{T_p}, shown in Figure 3.2. It can be seen that in general the thrust components, K_T and K_{T_p} decreases for increasing advanced coefficients, so is the propeller torque. It can be noticed as well that the total thrust of the thruster K_T has a higher value than the propeller thrust K_{T_p}. This seems odds since the the propeller is the only component of the thruster that delivers work. This definition of the force distribution will be discussed in detail in chapter 4. The reason for the total thrust to have a steeper slope has to do with the nozzle. At lower advance coefficients the presence of the nozzle results in higher total thrust, while for higher advance coefficients this positive effect of the nozzle on the thrust will reduce, because the drag of the nozzle will be more significant. The efficiency curve based on the total thrust, denoted by η_0, shows an increase for higher advance coefficients, till a maximum is reached. In this case the maximum lays at an advance coefficients of just above J=0.6. After this speeds the efficiency drops dramatically, therefore this working area is not that interesting anymore.

For the CFD calculations, the quasi-steady MRF-method was applied. The forces in the CFD-calculations are determined by the taking the surface integral of the pressure and shear forces acting on the surface of the thruster parts. The performance characteristics show a reasonably good agreement over the whole range of operation conditions from bollard pull to free sailing condition. Since the propeller torque is represented as $10K_Q$, the error is also 10 times enlarged. Still the relatively large difference in $10K_Q$ is most probably caused by the multiplication of multiple variables needed for the calculation of the propeller torque. Relatively small deviations within the variables may lead to relatively large differences compared with the experimental results. Overall, according to these results the numerical model seems to capture the flow field well, at least for this straight inflow condition.
The major difference between the fine and the coarse mesh configuration is that the local refinements are less fine. This will reduce the cell number to about one-third of the

fine model, a drawback is that it will be less accurate. Comparing the results between the fine and the coarse mesh, the coarse mesh results show only a small deviation with respect to the fine mesh results. Still the trends of the performance curves are captured quite well. Similar trends of this good agreement are found for the performance curve at a shaft speed of 16 rps, see Figure A.1. Hence, despite the small decay in accuracy, but with the advantage of a computational time drop of about two-third, it is decided that the coarse mesh gives sufficient insight in the occurring phenomena around the thruster. Further simulations will therefore be carried out using this mesh configuration.

3.3 Oblique Inflow Results

3.3.1 Quasi-Steady Results

The experiments with a varying oblique inflow were performed for four different operating conditions. Two different shaft speeds, 10.8 and 12 rps, and two different advance speeds, 0.901 and 1.422 m/s, were used, corresponding to J=0.30, J=0.33, J=0.47 and J=0.53. The condition at an advance speed of 1.422 m/s and shaft speed of 12 rps, corresponding to J=0.47, is shown in Figure 3.3. In these performance graphs the coefficients are plotted as a function of the heading angle δ. Moreover, a few extra forces and moments start playing a significant role. For instance the side force and the steering moment of the thruster unit, represented by K_{F_x} and K_{M_y}.

For the CFD results using the method of MRF, a good agreement with the experimental results is achieved over the whole range of heading angles. This is not the case for the steering moment K_{M_y}, which shows some abnormal results. Especially, the relative large

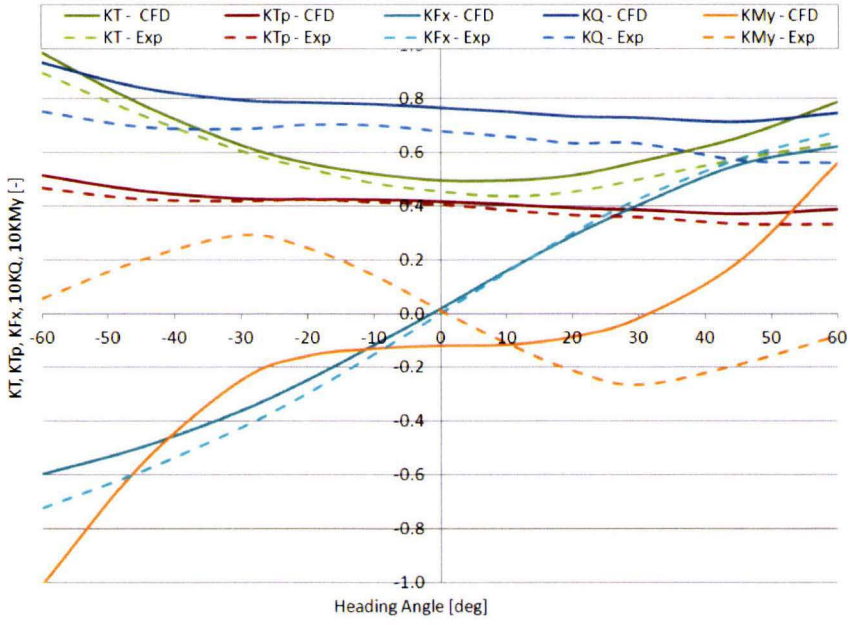

FIGURE 3.3: Comparison of the model scale experimental data with model scale CFD results using MRF, for oblique inflow (J=0.47).

value of steering moment for straight inflow is not plausible. The cause of this is that for the MRF-method the interaction between the shank and the propeller is determined for just one position of the propeller. Therefore the loading on the blades is unequal, which results in eccentric thrust production of the propeller. This phenomena, discussed in detail in section 5.2.2, leads to this steering moment K_{M_y} for straight inflow, even when there is no side force K_{F_x} present. The use of the MRF-method is therefore not suitable for the approximation of the steering loads for straight as for oblique inflow conditions.

3.3.2 Transient Results

Figure 3.3 showed that the method of MRF did not match the experimental data for the steering moment. Therefore the moving mesh method is applied to see whether this results in a better agreement, especially for the steering moment. The open water results proved that the coarse mesh was in good agreement with the open water experimental data. Since this fully transient method will cost about 6 times more computational time as the MRF-method, the use of the coarse mesh will save up to two-third of the total calculation time compared with the fine mesh simulations. The MRF results will be used as initial conditions for the MM simulations. Another additional phenomena that occurs due to the MM method, are the fluctuations in the results caused by the varying propeller orientations every time step, see Figure 3.4. These fluctuations are caused by a propeller blade passing the thruster house. In the considered case, the maximum blade loading corresponds to the position where the blade is behind the shank (Figure 1.1). It can be seen that it costs about two revolutions for the solution to get periodic. To get mean values for the performance characteristic, the results are averaged over one propeller revolution. The transient results for oblique inflow conditions are shown in Figure 3.5.

As was the case for the MRF results, the MM results for the propeller thrust, torque, total thrust and the side force show a good agreement with the experimental data.

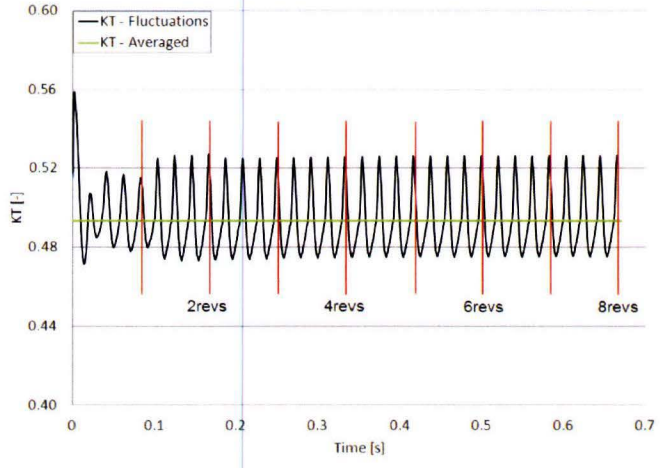

FIGURE 3.4: Total thrust fluctuation caused by the propeller blade passing the thruster house for δ=0, J=0.47.

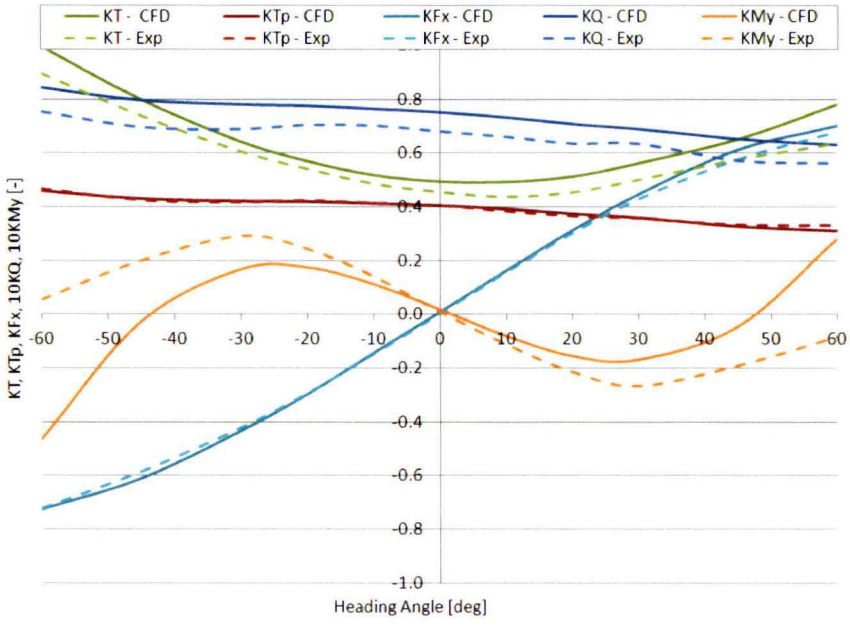

FIGURE 3.5: Comparison of the model scale experimental data with model scale CFD results using MM, for oblique inflow (J=0.47).

It shows even better results for the propeller thrust and torque at δ=0 than for the MRF-method.

Again the CFD results for the steering moment show some differences. It is not clear whether this deviation is caused by a small difference in the advance speed, between the experiment and CFD, or that the values of the steering moment actually differ. This will be explained in more detail in section 5.2.2. However, there is a much better qualitative agreement over the whole range of heading angles. The other three operating conditions show more or less the same agreement (Figure B.1, B.2, B.3). Hence, it is assumed that this numerical model is a good method to get insight in the loads and performances of a steerable thruster.

Chapter 4

Behavior of the Various Thruster Components

The validation of the numerical model shows that a good prediction can be established with the presented RANS-CFD method. Another interesting advantage of using CFD for the analysis of the behavior of a thruster is that numerical methods are very well suited to analyse the different components of a thruster unit. Contribution of the forces and moments, which act on each separate part, can be investigated. In order to make a distinction between the various parts of the thruster, somewhat more explanation is required. It may be clear that the thrust of a unit is produced only by the propeller, since the propeller is simply the only part that delivers work. Therefore, it may be confusing to state that other parts deliver thrust as well. Despite this it is common practice, for instance to attribute a certain amount of thrust to the nozzle. This thrust is not really delivered by the nozzle, because a static object is not capable of creating thrust. It is merely the result of pressure and shear forces of the fluid surrounding the nozzle, due to the action of the propeller.

4.1 Hydrodynamic Steering Moment

In the previous chapter it was mentioned that in case of oblique inflow, the side force and the steering moment starts to play a more significant role. For better understanding of this hydrodynamic steering moment, the underlying physical phenomena needs to be explained. The equation to determine the steering moment was already giving in section 1.3:

$$M_y = M_{zx} + M_{xz} = T \cdot r_x + F_x \cdot r_z \tag{4.1}$$

The first contribution is steering moment that arises from the eccentricity r_x of the thrust T. This component of the steering moment is called the thrust eccentricity moment. It is caused by the asymmetric inflow to the thruster, so the center of thrust is not exactly at the propeller axis. This behavior will be discussed in more detail in chapter 5.2.2.1.

The second component of the steering moment is caused by the appearance of a side force. This side force moment arises due to the drag forces of the water flow against the different parts of the thruster unit. At straight inflow this force is more or less balanced between the left and the right side of the thruster unit. For oblique inflow this will not be balanced anymore and therefore creates a moment around the steering axis. In Figure 4.1 a sketch is made to illustrate the contributing forces to the total hydrodynamic steering moment of the thruster unit. The location and direction of these forces show a typical situation: both contributing forces to the total steering moment are balanced to a certain extent.

To gain insight in these two hydrodynamic steering moment components, they need to be decoupled in the CFD package as well. A standard moment report function predefined in Starccm+, automatically adds the calculated values of the steering moment components $T \cdot r_x$ and $F_x \cdot r_z$. Therefore the individual components needs to be implemented by hand. The same underlying theory is used as for the standard report, based on the local pressure and the wall shear stress at the surface area of a cell. Decoupling of these forces in the required directions leads to the individual components of the steering moment.

4.2 Contribution of the Thruster Parts

As discussed before, it is possible to divide the thruster unit into multiple parts, so the performance of each individual part can be determined. For the four different operation conditions J=0.30, J=0.33, J=0.47 and J=0.53, which were compared with the experiments using the MM-method, more or less the same behavior is seen for each condition. Therefore only one condition with a shaft speed of 12 rps and an advance speed of 1.422 m/s, corresponding to J=0.47, will be treated in detail. In Figure 4.2 and 4.3 the performance in thrust, K_T, and side force, K_{F_x}, are shown.

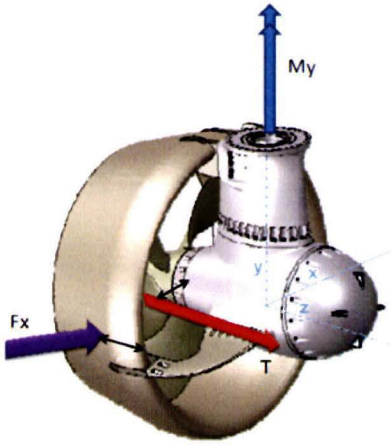

FIGURE 4.1: The underlying contributing forces to the hydrodynamic steering moment.

Analysis of the thrust coefficient shows a result which is not entirely unexpected. It can be clearly seen that the thrust is mainly produced by the propeller and the nozzle. The other parts only provide a certain amount of resistance, because they deliver a negative value of thrust. As expected, the total thrust coefficient increases for larger heading angles, because the component of the incoming advance velocity in the direction of the propeller axis decreases. Comparable behavior is seen for the open water characteristic in Figure 3.2, where the thrust also increases when going from free sailing to the bollard pull condition (zero speed). It is obvious, looking at the graph, that the increase in total thrust is mainly due the nozzle. The influence of the nozzle on the total performance of the thruster unit is even more apparent when looking at the side force coefficient. Figure 4.3 shows that the shape of the total side force curve is to a large extent, due to the effect of the nozzle.

The same is true for the extent in which the nozzle contributes to the components of the hydrodynamic steering moment, Figure 4.5 and 4.4. The nozzle and the propeller, are furthest away from the steering axis and so is the arm corresponding to the side force F_x. This causes the side force moment to be almost only dependent of the nozzle, as the side force of the propeller is small. For the thrust eccentricity moment the thrust is produced by the propeller as well as the nozzle. But the thrust eccentricity of the propeller is very small, as will be shown in chapter 5.2.2.1. This component of the hydrodynamic steering moment will therefore mainly be allocated to the nozzle as well. To visualize this, the pressure distribution on the thruster unit is shown in Figure 4.6 and 4.7, for a 0 degree heading angle and a -30 degree heading angle. The pressure distribution clearly shows the difference between both sides of the nozzle. This indicates the eccentricity of the nozzle thrust. Whereas the pressure distribution on the propeller for the two condition shows more or less similar results.
Furthermore, it can be seen that both steering moment components are balanced to a certain extent. This leads to the particular behavior of the total hydrodynamic steering moment, which will be discussed in more detail in chapter 5.2.2.

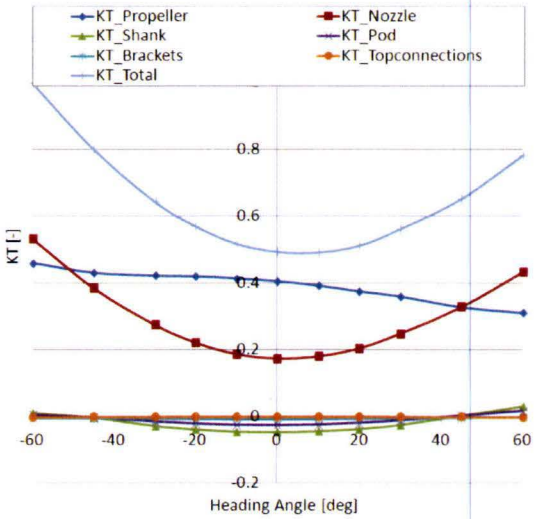

FIGURE 4.2: Thrust coefficient of the different parts for oblique inflow.

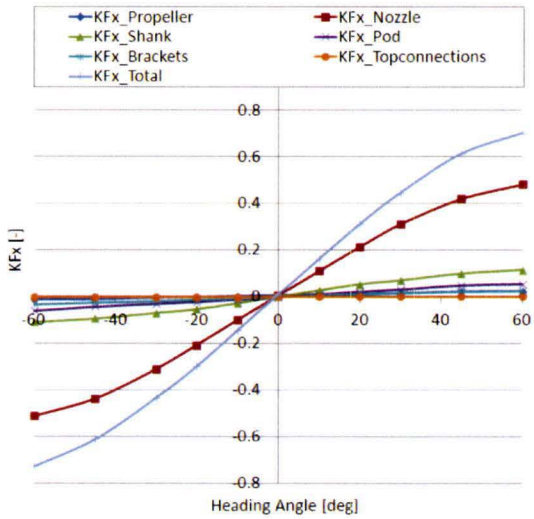

FIGURE 4.3: Side force coefficient of the different parts for oblique inflow.

Overall, it can be seen that the loading of the thruster unit, especially side force related loading, is dominated by the presence of the nozzle. Amini and Steen [1], who performed a experimental and theoretical analyses of propeller shaft loads for oblique inflow about the same behavior of the performance characteristics of the thruster unit is found, but for a thruster unit with an open propeller, without the existence of the nozzle.

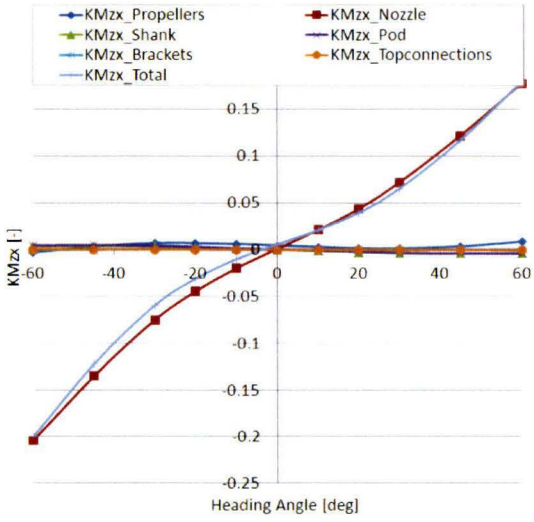

FIGURE 4.4: Thrust eccentricity coefficient moment of the different parts for oblique inflow.

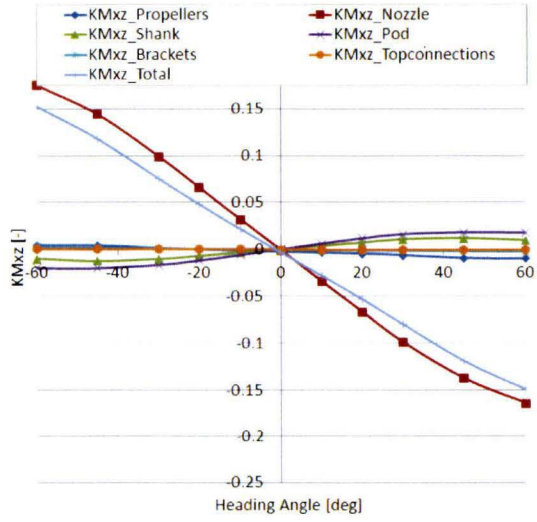

FIGURE 4.5: Side force moment coefficient of the different parts for oblique inflow.

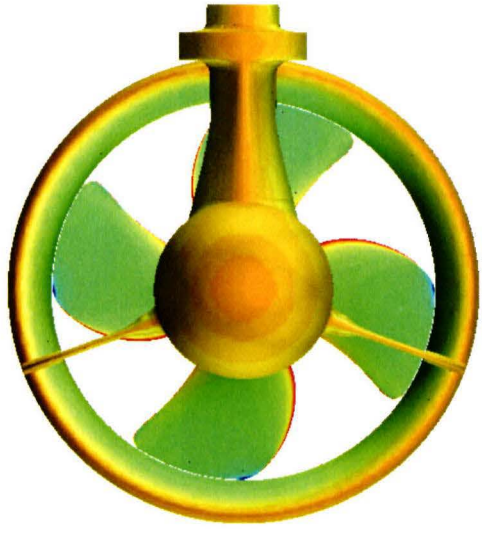

FIGURE 4.6: Pressure distribution on a the thruster for heading angle δ=0.

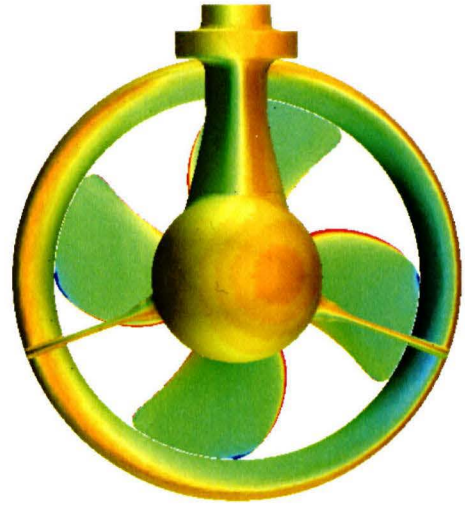

FIGURE 4.7: Pressure distribution on a the thruster for heading angle δ=-30.

Chapter 5

Behavior of the Thruster Unit

In chapter 4 the evaluation of the results of the different parts of a thruster showed that the propeller and the nozzle are the most important parts contributing to the forces on a steerable thruster. For the analyses of a thruster unit and its steering moment, the range of advance coefficients is now extended to range of J=0 to J=0.76. For this case a propeller rotation rate of 12 rps is used. Also the range of heading angles is extend to 90 degrees in both negative and positive heading direction. To understand the behavior of the thrust, it will be discussed in a few constructive steps.

5.1 Force Analysis

5.1.1 Thrust

At first the influence of the change in advance speed, for straight inflow conditions, will be explained by the underlying theory of a propeller blade. According to the open water diagram, Figure 3.2, a reduction in advance speed, results in an increase in propeller thrust K_{Tp} and torque K_Q. The underlying physical phenomenon of this has to do with the angle of incidence α of the blade section. The thrust and torque of a propeller follow from the integration of lift and drag forces over the span of the propeller blades. These lift forces are determined by the area, the fluid density, the velocity and the lift coefficient. The lift coefficient increases with increasing incidence angle α. To discuss this, the forces on a propeller blade are shown in 5.1. Neglecting the induced velocity, the angle of incidence can be derived from the blade angle θ and the inflow angle ϕ of the water onto the propeller rotation plane. This angle ϕ should not be confused with the oblique inflow angle δ.

$$\begin{aligned} \alpha &= \theta - \phi \\ &= \theta - \tan\frac{V_a}{\omega r} \\ &= \theta - \tan(\pi J) \end{aligned} \tag{5.1}$$

Here ω is the angular velocity of the propeller and r the radius of the blade section to the propeller axis.

It can be seen from the graph that the lift L_{blade} and drag D_{blade} forces of the propeller blade are perpendicular to and aligned with in the inflow angle ϕ of the fluid. Therefore the thrust of the blade section T_{blade}, can be written as follows:

$$T_{blade} = L_{blade}\cos(\phi) - D_{blade}\sin(\phi) \tag{5.2}$$

So, decreasing the velocity leads to an increase in angle of incidence. This leads to an increase in lift. Also the magnitude of drag force will increase, but is more pointing in the rotation direction. On the other hand the total velocity will show a decrease as well. Therefore, it is not straight forward to say that a decrease in velocity, directly results in a thrust increase. Still Figure 3.2, shows this behavior. This means that the constant rotational speed component of the propeller is the leading component. Therefore, the change of the inflow angle ϕ of the water onto the propeller rotation plane dominates the change of the total velocity. Hence, decreasing the advance speed results in an increase thrust.

Secondly the behavior of thrust for varying heading angles δ will be discussed. Putting the thruster unit into an azimuth position to the flow the axial inflow velocity will decrease, which increases the angle of incidence α. This shall result in an increase in thrust. This can be seen in a simplified sketch of the situations at the upper and lower part of the propeller plane for a positive heading angle, Figure 5.2. With ωr the tangential velocity of the propeller, $\vec{V}$ the velocity of the flow and $\vec{W}$ the relative velocity.

Besides this, it can be observed that the relative tangential velocity W_x and the angle of incidence α vary for the upper and lower plane. Changing to a negative heading angle shows that the two sketched situations will switch sides. The upper plane of the positive

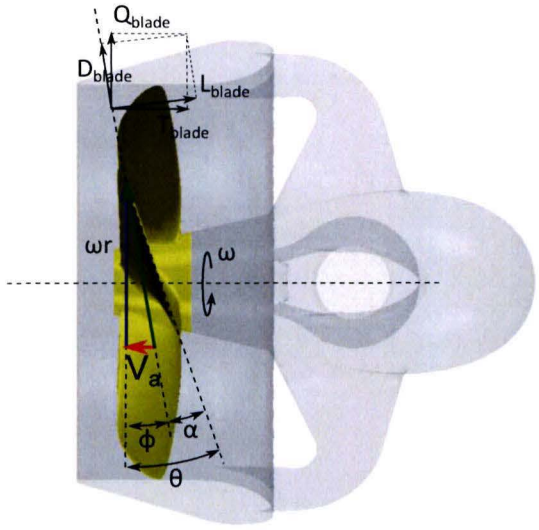

FIGURE 5.1: Force balance of a propeller blade.

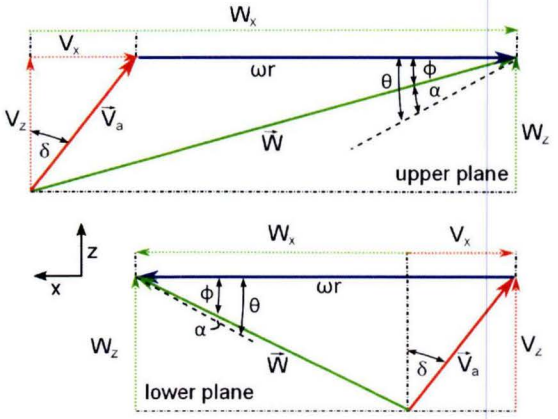

FIGURE 5.2: Velocities triangles at the upper and lower propeller plane.

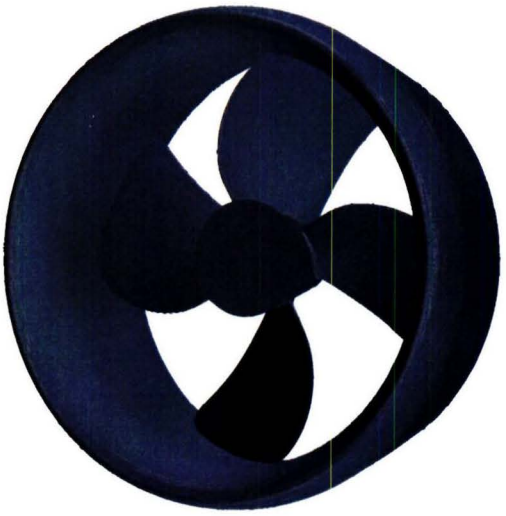

FIGURE 5.3: The adapted thruster model, without thruster house.

heading angle, becomes the lower plane of the negative heading angle. Assuming the switch between the lower and upper plane for negative and positive angles, the absolute situation at the overall in-plane velocities should not differ. Therefore the results for negative and positive heading angles will be the same, independent of the rotation direction of the propeller.

To verify this, the original thruster unit is adapted, consisting of only the propeller and the nozzle, see Figure 5.3. With this model a uniform oblique inflow in the propeller plane is created, at least for the smaller heading angles. Before analyzing the oblique inflow results, the performance characteristics at δ=0 are compared with the original model in Figure 5.4. The results show that the appearance of the thruster house for straight inflow conditions has almost no effect on the performance of the thruster unit. The results seems to be in good agreement, which gives the possibility to compare the results for oblique inflow conditions.

In Figure 5.5 and 5.6 the results for varies heading angles δ and advance coefficients are shown for the adapted model. It can be seen that the thrust results are equal for negative and positive heading angles, except for the higher heading angles 75° and 90°, where the propeller is partly or totally in the shadow of the nozzle. This together with the rotation direction of the propeller, results in a difference in thrust for these heading angles.

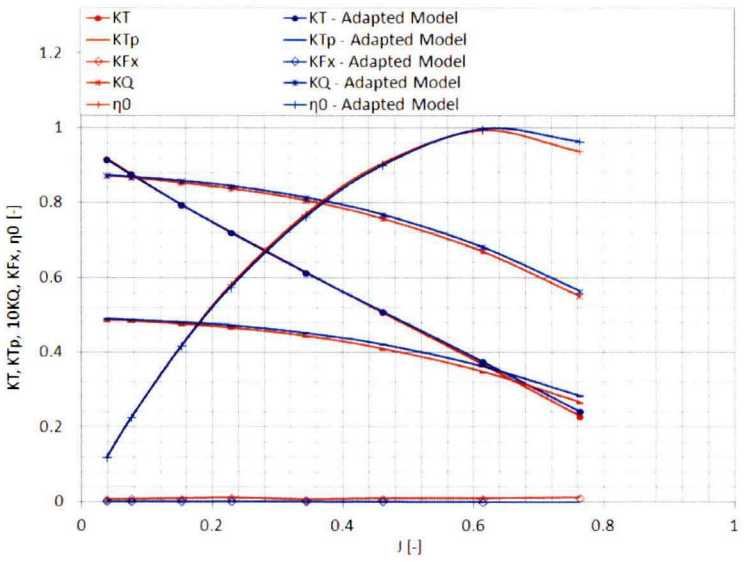

FIGURE 5.4: Open water comparison between the original and adapted model.

It can be seen as well that the behavior of the total thrust coefficient K_T increases for increasing heading angles δ. As already mentioned before, the thrust will be affected, because of reduction in the axial inflow velocity due to the azimuth position of the thruster unit with respect to the incoming flow. In Figure 5.5 it can also be seen that for higher heading angles, the thrust reduction for increasing advance coefficients is less than for lower heading angles. The reason for this behavior are the changes in the angle of incidence. These results are in line with the Glauert's theory [6] for propeller blades in oblique inflow conditions.

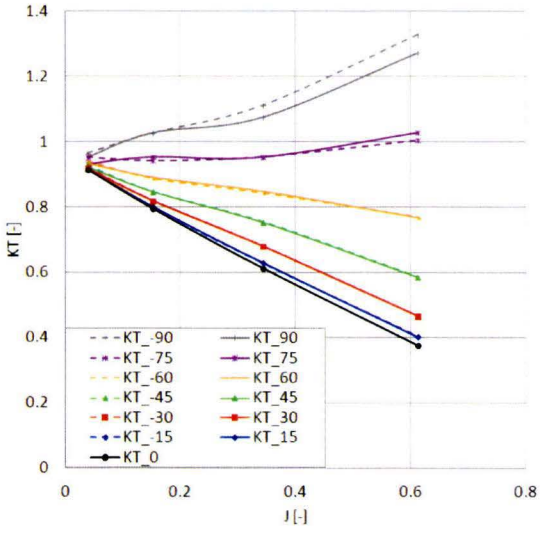

FIGURE 5.5: Total thrust at various heading angles δ, for varying advance coefficients J, for the adapted model

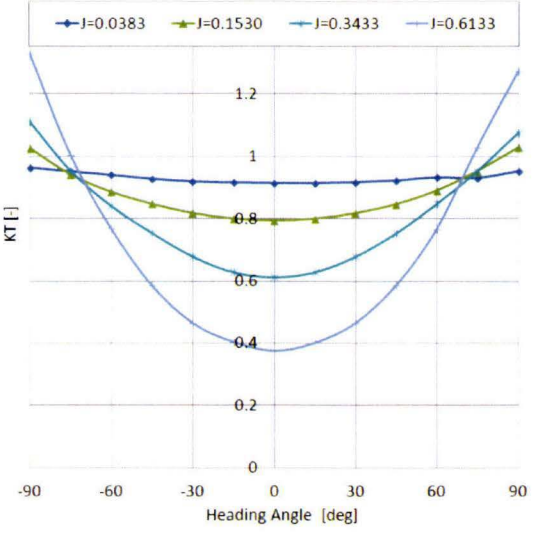

FIGURE 5.6: Total thrust at various advance coefficients J, for varying heading angles δ, for the adapted model.

The effect of the change in advance coefficients and heading angles is now seen for a uniform inflow (Figure 5.5 and 5.6). For the original thruster unit, this uniform inflow is disturbed by the thruster housing. The influence of the thruster house with respect the total thrust of the unit is shown in Figure 5.7 and 5.8. It is possible to see a difference between negative and positive heading angles. The presence of the thruster house, including the pod, shank, top and bottom connections, is partly blocking the incoming fluid flow. Together with the rotating direction of the propeller this asymmetry for negative and positive will be explained. For azimuth configurations the influence of the blockage of the thruster house will change the velocity distribution at the propeller plane, as will be visualized in section 6.2. This disturbance of the flow field will cause a difference for the negative and positive heading directions. For both positive and negative heading angles, the thruster house leads to a reduction in the overall in-plane velocity on the upper part of the propeller plane. This means that the influence of the lower propeller plane becomes more significant. Therefore, for positive heading angles the total overall in-plane velocity at both the upper and lower propeller plane, induces a tangential velocity component that acts in the opposite direction of the propeller rotation. This results in a thrust reduction, while for negative heading angles the opposite occurs. This tangential velocity induced by the overall in-plane velocity on the upper side of the propeller plane acts in the opposite direction of the propeller rotation, resulting in a thrust increase.

For sailing purposes is may be more interesting to look at the thrust in the sailing direction. The thrust in sailing direction is also probably more in line with the expectation that steering a thruster unit reduces the thrust in the heading direction. In Figure 5.9 and 5.10, the thrust in sailing direction is shown for varying advance coefficients and heading angles.

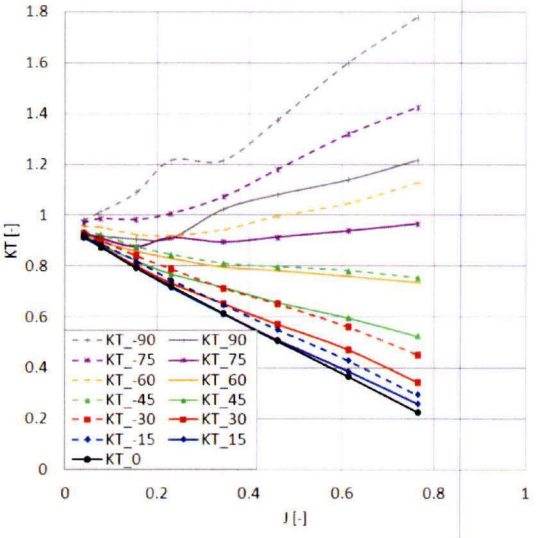

FIGURE 5.7: Total thrust at various heading angles δ, for varying advance coefficients J.

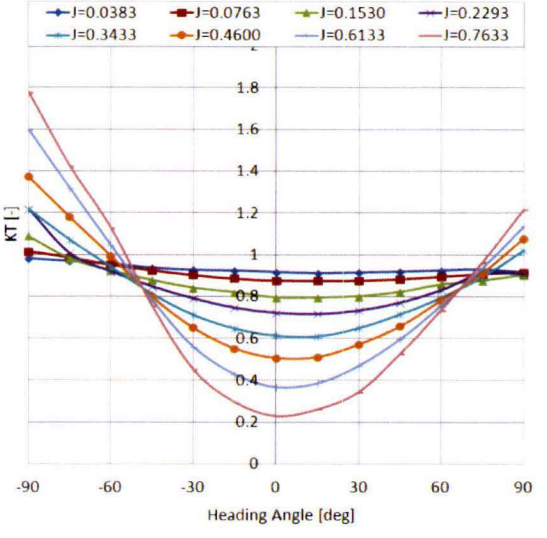

FIGURE 5.8: Total thrust at various advance coefficients J, for varying heading angles δ.

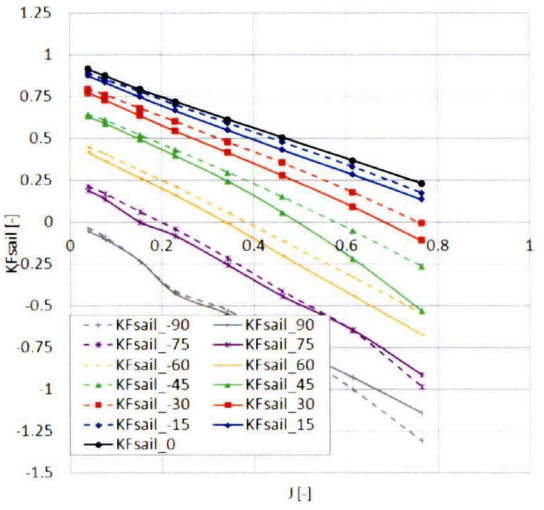

FIGURE 5.9: Thrust in sailing direction at various heading angles δ, for varying advance coefficients J.

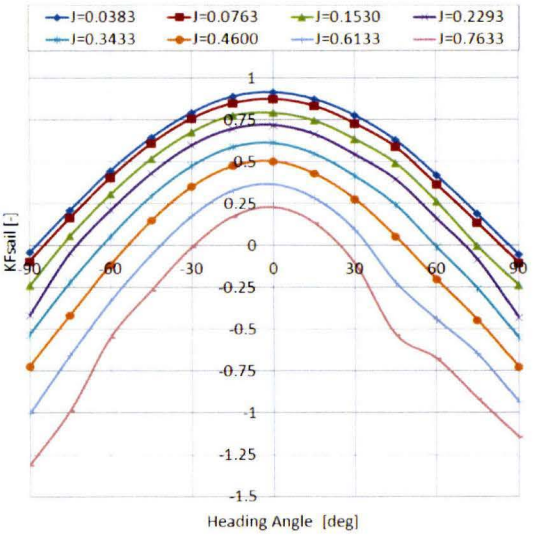

FIGURE 5.10: Thrust in sailing direction at various advance coefficients J, for varying heading angles δ.

For increasing advance coefficients for straight inflow conditions δ=0, the thrust in sailing direction is equal to the thrust in the axial direction. An increase in velocity leads to a decrease in thrust. Rotating the thruster unit to an angle towards the flow, results in a decrease in thrust. For lower advance coefficients the thruster will, almost over the whole range of heading angles, deliver a certain amount of thrust. Increasing the advance coefficient shows that the thrust in sailing direction will become negative. This negative thrust means that the lift created by the propeller is less than the drag forces of the thruster. Therefore, the thruster will not deliver thrust in the heading direction for higher heading angles and velocities, but only a drag force.

5.1.2 Side Force

The side force of a steerable thruster is mainly caused by the acting loads of the water onto the nozzle, the drag forces. The side force for various heading angles and advance coefficients is shown in Figure 5.11 and 5.12. In Figure 5.11 the absolute value of K_{F_x} is denoted. It is not surprising to see, since a drag force is strongly dependent of the x-velocity, raising the advance coefficient results to a increase in the x-velocity and thus the side force will higher as well for oblique inflow conditions.

It can also be seen that there is a small difference between the negative and positive heading angles. The non-zero side force at for straight inflow, seems to have an effect on the side force at oblique inflow conditions. This results in a slightly decrease in side force for the negative heading angles and a slightly increase for the positive heading angles.

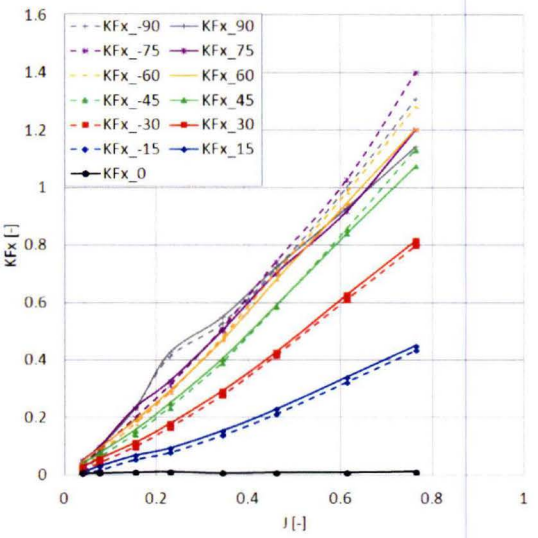

FIGURE 5.11: Side force at various heading angles δ, for varying advance coefficients J.

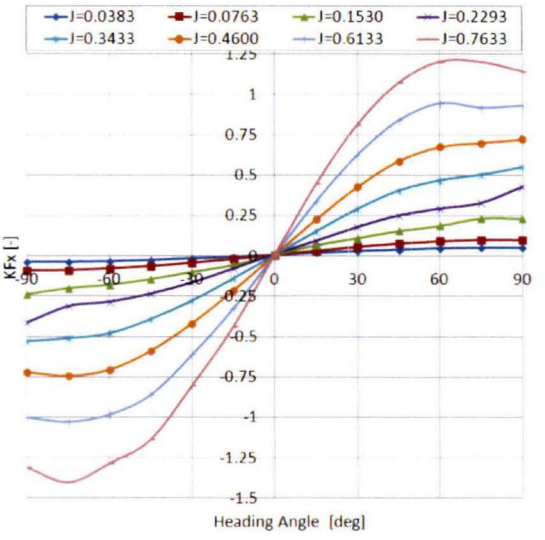

FIGURE 5.12: Side force at various advance coefficients J, for varying heading angles δ.

5.2 Moment Analysis

5.2.1 Propeller Torque

Figure 5.13 and 5.14 show the torque coefficient of the propeller $10K_Q$ for various heading angles and difference advance coefficients. It had been observed in figure 3.2, that the propeller torque decreases for increasing advance coefficients for straight inflow conditions δ=0. Since the propeller torque is mostly dependent on the propeller thrust, this is an expected result. It can be seen is that the results show a difference for negative and positive heading angles. For positive heading angles the propeller torque is lower with respect to the straight inflow condition, while for negative heading angles the propeller torque shows a higher value. This is related to the rotating direction of the propeller. It can also be seen that the propeller torque for higher heading angles shows different behavior than for lower heading angles. This is caused by a reduction in mass flow through the nozzle for these higher heading angles, as will be seen in Figure 6.10.

5.2.2 Hydrodynamic Steering Moment

Due to steering, the thruster operates at oblique inflow conditions. The hydrodynamic loads will become significant, especially for higher advance coefficients. The behavior of the hydrodynamic steering moment acting on the thruster unit is shown in Figures 5.15 and 5.16. The trend of the steering moment shows some typical behavior. In Figure 5.16, for lower advance coefficients it seems to be a linear increase in moment for increasing heading angles, while the behavior for higher advance coefficients show a sine-like trend. This behavior in overall steering moment indicates that there are two different components playing a role. As discussed in section 5.2.2 these two components

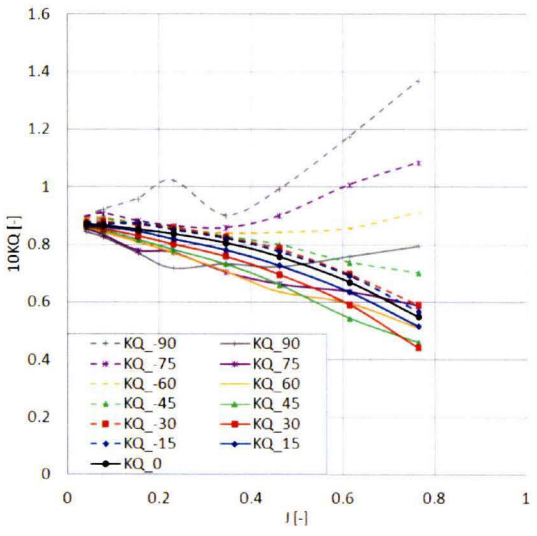

FIGURE 5.13: Propeller torque at various heading angles δ, for varying advance coefficients J.

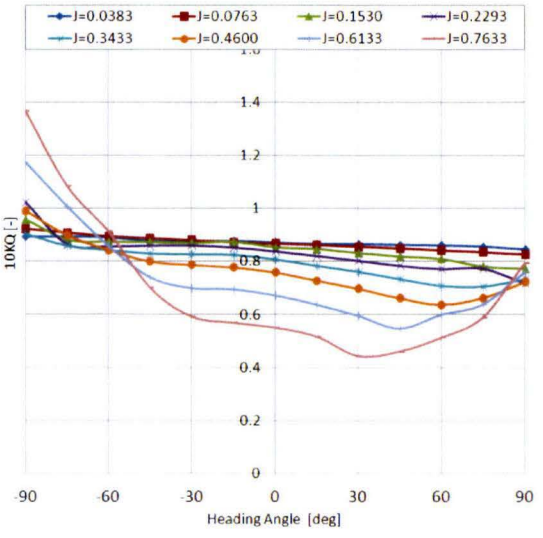

FIGURE 5.14: Propeller torque at various advance coefficients J, for varying heading angles δ.

of the steering moment are due to the thrust eccentricity moment and the moment induced by the side force. It is most likely that the maximum of the overall steering moment at about 30 deg, is caused by a dominance of the thrust eccentricity for low J-values. While for high J-values, the contribution of the side force moment that becomes dominant over the thrust eccentricity moment, because of a rapid increase in side force F_x for higher velocities.

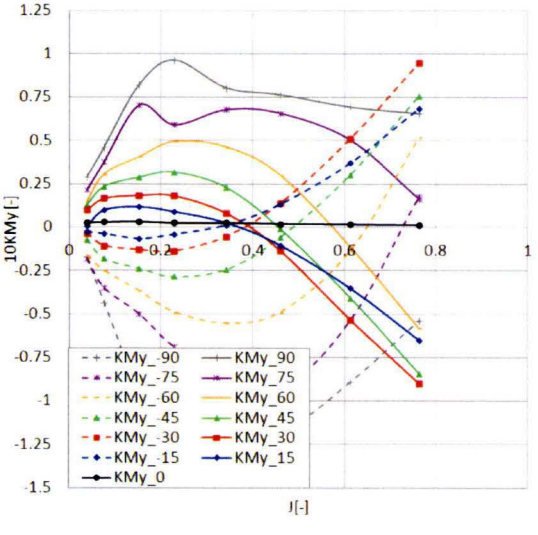

FIGURE 5.15: Hydrodynamic steering torque at various heading angles δ, for varying advance coefficients J.

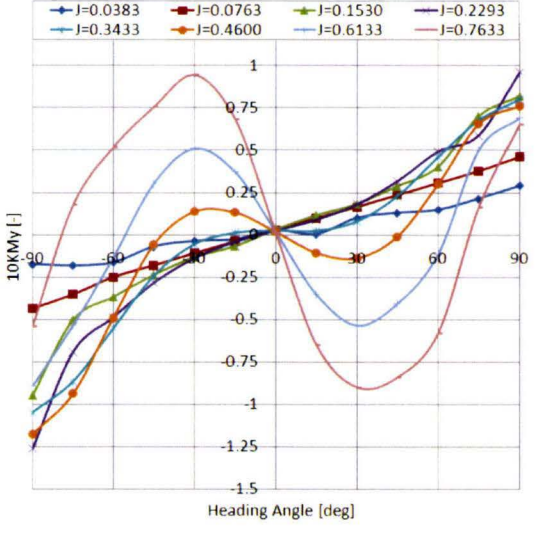

FIGURE 5.16: Hydrodynamic steering torque at various advance coefficients J, for varying heading angles δ.

Since both steering moment components are important for the hydrodynamic steering moment, the thrust eccentricity moment is shown in Figure 5.17 and 5.18, the side force moment is shown in Figure 5.19 and 5.20. It can be seen, since both components have more or less the same magnitude and sign, that the absolute value of the overall steering moment will be lower, according to equation 4.1.

The contribution of the thrust eccentricity moment increases for high advance coefficients J and for higher heading angles. Both phenomena could be explained by the higher thrust for lower axial velocities to the propeller plane. Lower axial velocities lead to an increase in thrust as is already seen in several open water diagrams. The increase in contribution of side force component could specifically be related to a raise in x-velocity due to an higher advance coefficient J. The existence of those two components of the steering moment could be a reason for the deviation between the experimental and the numerical results. Rather small differences could lead to a relatively large difference in the overall hydrodynamic steering moment.

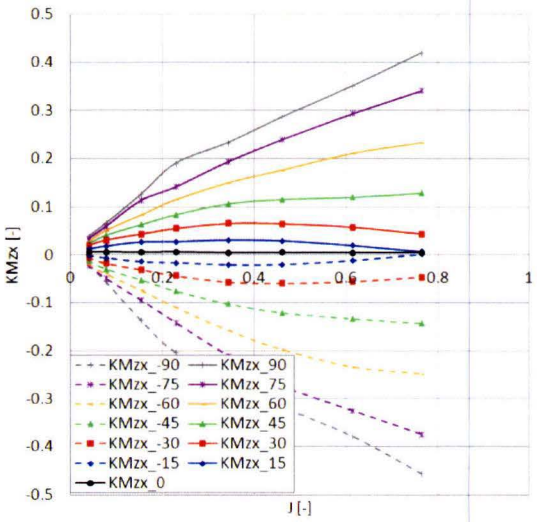

FIGURE 5.17: Thrust eccentricity moment at various heading angles δ, for varying advance coefficients J.

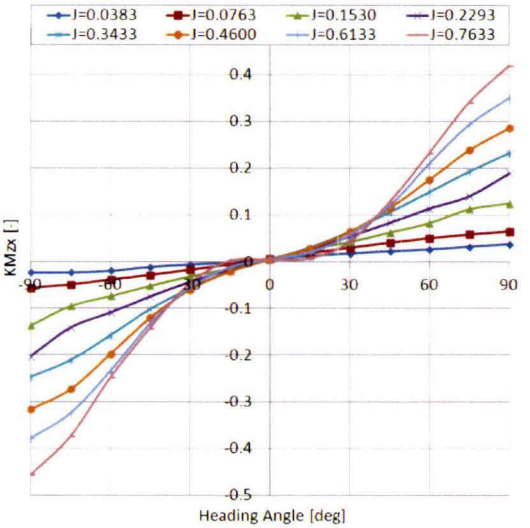

FIGURE 5.18: Thrust eccentricity moment at various advance coefficients J, for varying heading angles δ.

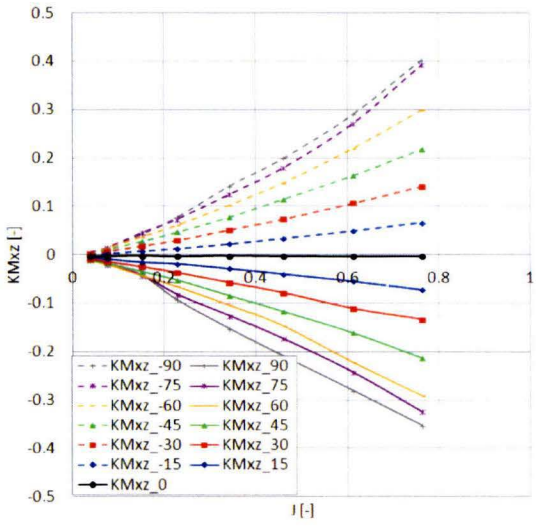

FIGURE 5.19: Side force moment at various heading angles δ, for varying advance coefficients J.

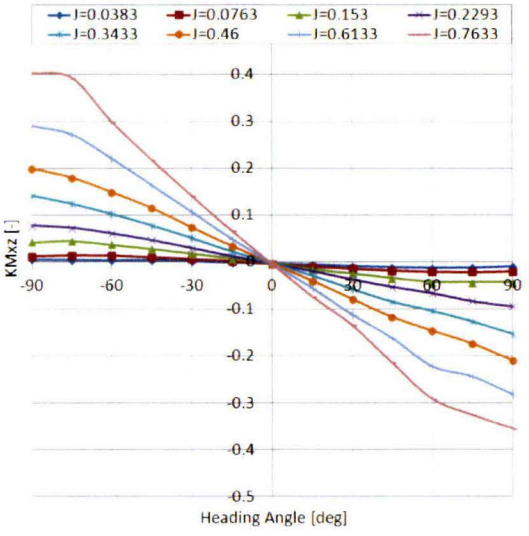

FIGURE 5.20: Side force moment at various advance coefficients J, for varying heading angles δ.

5.2.2.1 Thrust Eccentricity

For the thrust eccentricity component the center of thrust moves away from the propeller axis, leading to a bending moment. This thrust eccentricity occurs due to the oblique inflow at nozzle, because of the angle of the thruster to the incoming flow. In Figure 5.21 the thrust eccentricity is illustrated, presented as a percentage of the propeller radius R. Only the propeller and the nozzle eccentricity are shown, because those parts of the thruster unit are responsible for the majority of the thrust. The arm is found by dividing the thrust eccentricity component of the steering moment by the corresponding thrust. It seems that the thrust center of the propeller stays more or less at the center of the propeller. While the center of thrust of the nozzle shows a significant movement, ensuring that this steering moment is mainly caused by the nozzle. The arm increases for higher advance coefficients or heading angles, to a maximum of about the radius of the propeller. The increasing value for the thrust eccentricity for higher advance coefficients is sufficient to cause an increase of the steering moment over the whole range of heading angles, even though the thrust is less for higher advance coefficients. It seems that for higher heading angles the propeller has a small eccentricity as well. In those conditions the propeller is for some extent behind the nozzle, which shows an eccentric thrust production for the propeller.

5.2.2.2 Arm of the Side Force Moment

The side force, as was shown in section 4.2, is mainly produced by the nozzle. Therefore, the contribution of the propeller in side force moment is more or less negligible and the focus will only be on the nozzle part. the length of the lever-arm r_z of the side force moment is shown in Figure 5.22, represented as the percentage of the distance from the steering axis to the propeller. This figure shows that the advance coefficient does not have much influence on the arm. For the thruster operating in oblique inflow conditions the length of lever-arm will slightly increase. Together with the increasing side force it provides a raising steering moment for higher heading angles. For straight inflow it seems that the arm has a minimum value compared with the azimuth operating condition. Most likely this is caused by the very small value of this moment and the side force for a zero degree angle. Hence, small deviations will results in relatively large changes for the value of r_z.

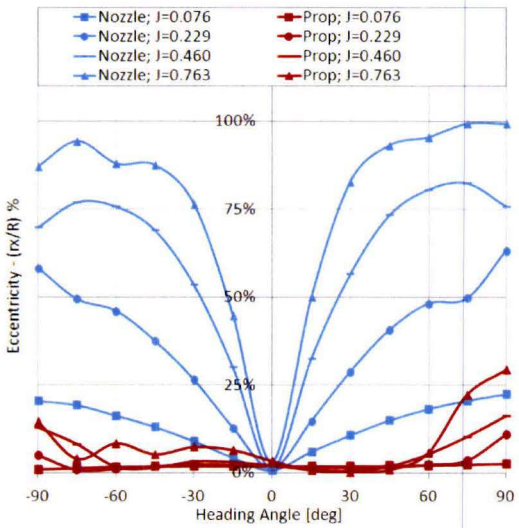

FIGURE 5.21: The thrust eccentricity of the propeller and nozzle, for various advance coefficients and heading angles.

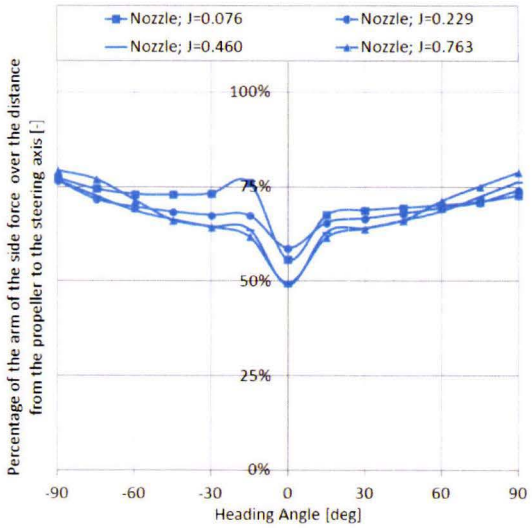

FIGURE 5.22: Length of the lever-arm of the side force of the nozzle, for various advance coefficients and heading angles.

Chapter 6

Influence of the Thruster Housing

Analyzing the results show that there is a certain asymmetry in most of the performance characteristics. Also some hydrodynamic steering moment was observed for the non steering condition, due to the side force induced by the thruster house. In this chapter the asymmetry between the negative and positive heading angles will be explained by qualifying different phenomena. This helps to get full understanding in the occuring behavior of the hydrodynamic loads on the thruster unit.

6.1 Asymetric Side Force for Straight Inflow Conditions

The presence of the thruster house for straight inflow conditions has almost no effect on the performance of the thruster unit. But, apparently the results for the thruster unit in combination with the propeller rotation has a small effect on the side force, since the side force is not exactly zero for the straight inflow condition, see Figure 5.11. In other words, the heading angle of where the side force is symmetric, is not exactly at $\delta = 0$. To compare the differences in the results for negative and positive heading angles, the side force should be zero at $\delta = 0$. A correction in the form of K_{F_x}-$K_{F_{x_0}}$ for the offset to get the sideforce symmetric for straight inflow is therefore implemented in the side force related results. $K_{F_{x_0}}$ respresents the side force at $\delta = 0$. The result is shown in Figure 6.1. It can be seen that the same deviation is occuring for small heading angles. Depending on the heading angle, negative or positive, this forces will contribute to the side force, or will counteract to the side force applied by the flow. Since this phenomena is occuring for lower heading angles, it is assumed that also for higher heading angles this phenomena is taking place.

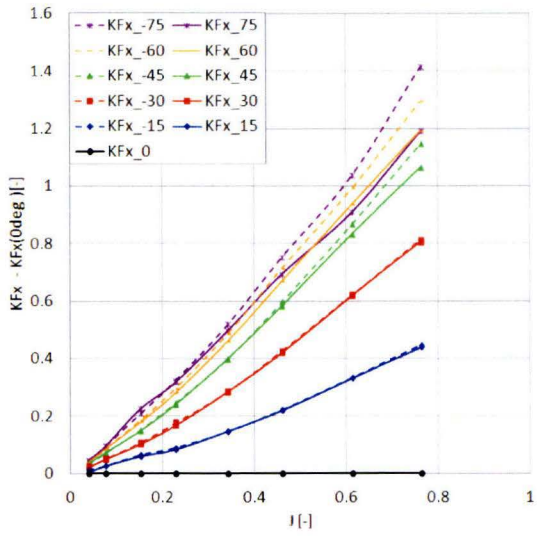

FIGURE 6.1: Corrected results for the asymetric side force.

6.2 Pre-Rotation of the Flow

It is already mentioned that the thruster house induces a certain tangential velocity component, influencing the performance of the propeller. In this case, this results for negative heading angles in a thrust increase, as for positive heading angles the thrust decreases (Figure 5.7). For undisturbed oblique inflow almost no difference in thrust was found between the negative or positive heading angles (Figure 5.5). The only difference will be that the velocity triangles from the upper and lower plane will switch, resulting in the same overall in-plane tangential velocity. The CFD results of the adapted model, so without the existence of the thrusterhouse, helps to visualize the in-plane velocities. This plane is determined just before the propeller, at the intersection of the rotating propeller domain. The massflow at the propeller plane does not change much for variing heading angles and advance coefficients except for heading angles higher than δ=60, see Figure 6.10. Hence, the focus will be on the tangential component of the velocity, instead of the axial component. Figures 6.2 and 6.3 show an example of the in-plane velocities at a particular propeller position, for a J-value with a local tangential velocity, for the heading angles δ=-30 and δ=30. A shaft speed of 12 rps and an advance speed of 1.38 m/s is used (J=0.46). The exchange between the upper and lower plane can clearly be seen. The averaged overall in-plane tangential velocity $\overline{V_t}$ results in a value of about $-3.0 \cdot 10^{-2}$ m/s in both cases.

Now, including the flow disturbance caused by the thruster house, will cause a change in tangential velocity distribution in the propeller plane, so are the corresponding advance coefficients, see Figure 6.4 and 6.5. It could be observed that distribution from the upper and lower side for negative or positive heading angles shows some differences.

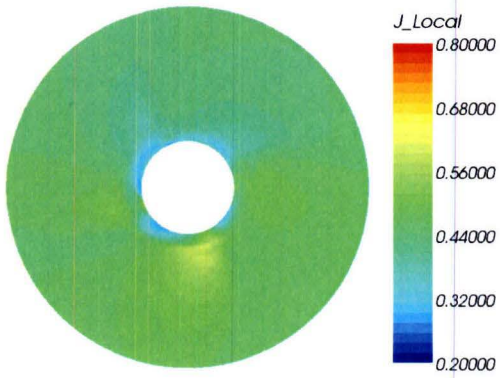

FIGURE 6.2: J, using local tangential velocity in the propeller plane at δ=-30, for undisturbed inflow.

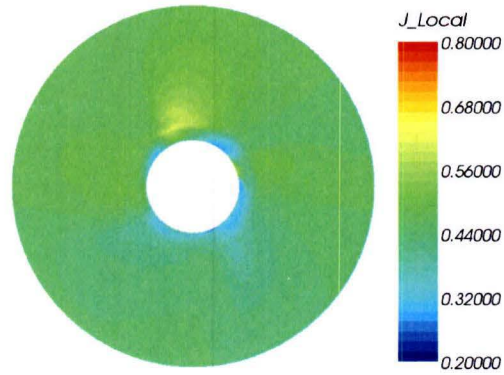

FIGURE 6.3: J, using local tangential velocity in the propeller plane at δ=30, for undisturbed inflow.

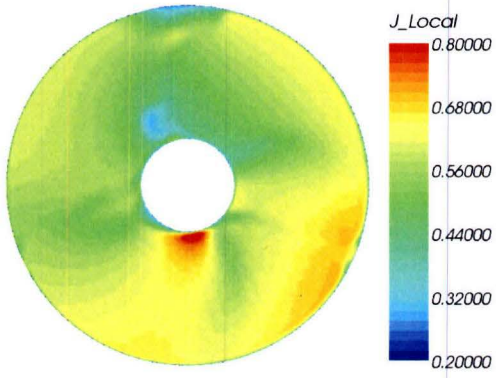

FIGURE 6.4: J, using local tangential velocity in the propeller plane at δ=-30, for disturbed inflow.

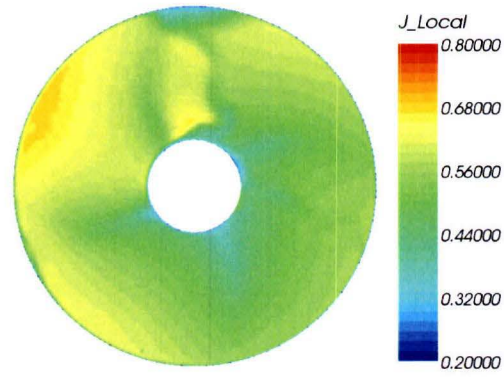

FIGURE 6.5: J, using local tangential velocity in the propeller plane at δ=30, for undisturbed inflow.

This results in a change in the average overall in-plane tangential velocity. In case of heading angle δ=-30, $\overline{V_t}$=1.3·10^{-1} m/s. In case of an heading angle δ=30, $\overline{V_t}$=-1.4·10^{-1} m/s.

By using equation 6.1, the relative angular velocity n_{eff} of the flow at the propeller plane can be calculated. This n_{eff} consists of the propeller rotation rate n and the averaged angular velocity, due to a pre-orientation of the flow with a certain direction, caused by the disturbance in the inflow Δn.

$$n_{eff} = n + \Delta n = n + \frac{1}{A} \iint_A \frac{V_t(r,\theta) \cdot 2\pi}{r} dA \tag{6.1}$$

It can be seen, looking at the tangential velocity at the propeller plane, that Δn is acting in opposite directions for negative and positive heading angles. Therefore, for negative heading angles this results in a slight increase in relative angular velocity. In case of an oblique heading angle of -30 degrees, the relative rotation rate at the propeller

increases from n=12 rps to n_{eff}=12.26 rps, corresponding to J=0.45. While for a positive heading angle of 30 degrees the relative rotation rate will decrease to n_{eff}=11.71 rps, corresponding to J=0.47.

Together with the shift in the side force for straight inflow the dimensionless terms can be modified. The flow phenomena occurring due to the presence of the thruster house could be taken into account using the following non-dimensional terms for the performance characteristics:

Effective advance coefficient	$J_{eff} = \frac{V_a}{n_{eff} D}$
Effective thrust coefficient	$K_{T\,eff} = \frac{T}{\rho {n_{eff}}^2 D^4}$
Effective torque coefficient	$K_{Q\,eff} = \frac{Q}{\rho {n_{eff}}^2 D^5}$
Effective efficiency	$\eta_{0\,eff} = \frac{J_{eff}}{2\pi} \frac{K_{T\,eff}}{K_{Q\,eff}}$
Effective side force coefficient	$K_{F_x\,eff} = \frac{F_x - F_{x_{0deg}}}{\rho {n_{eff}}^2 D^4}$
Effective steering moment coefficient	$K_{M_y\,eff} = \frac{M_y - M_{y_{0deg}}}{\rho {n_{eff}}^2 D^5}$
Effective thrust eccentricity moment coefficient	$K_{M_{zx}\,eff} = \frac{T r_x}{\rho {n_{eff}}^2 D^5}$
Effective side force moment coefficient	$K_{M_{zx}\,eff} = \frac{F_x r_z - F_{x_{0deg}} r_{z_{0deg}}}{\rho {n_{eff}}^2 D^5}$

Where $F_{x_{0deg}}$, $M_{y_{0deg}}$ and $r_{z_{0deg}}$ are respectively the side force, the steering moment and the arm of the side force at the straight inflow conditions. This are corrections for the offset of the values at a zero degree heading angle, but is also clearly recognizable for the lower heading angles, as mentioned in the previous section.

6.3 Results Using Modified Performance Characteristics

Using these effective dimensionless coefficients, the disturbance of the inflow at the propeller plane is taken into account. Therefore, the differences between the negative and positive heading angles should be corrected. In Figure 6.6 and 6.7 the differences are shown for the thrust using the normal coefficients from section 1.3 and the modified coefficients. Observing the two graphs show that the asymmetry in thrust for the modified characteristics is almost totally resolved. This results tells that the disturbance of the thruster house could be corrected using the effective advance coefficients J_{eff} of the incoming flow at the propeller plane.
Also the values for the propeller torque show good results using the corrected characteristics, see the comparison between Figure 6.8 and 6.9. The differences between the several heading angles are reduced considerably. As was seen in section 5.2.1 the propeller torque for the higher heading angles showed different behavior than for lower

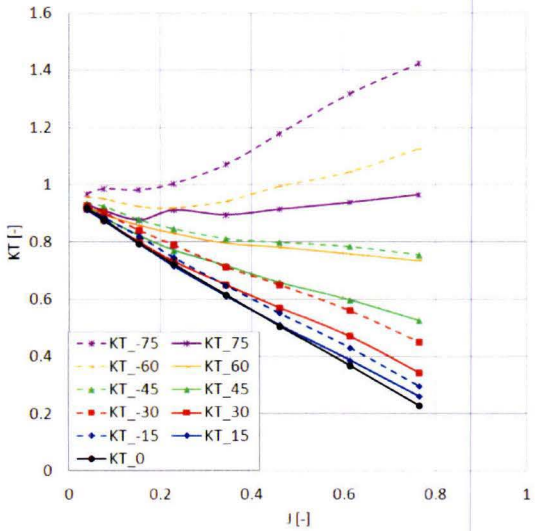

FIGURE 6.6: Thrust for various advance coefficients and heading angles, using normal coefficients.

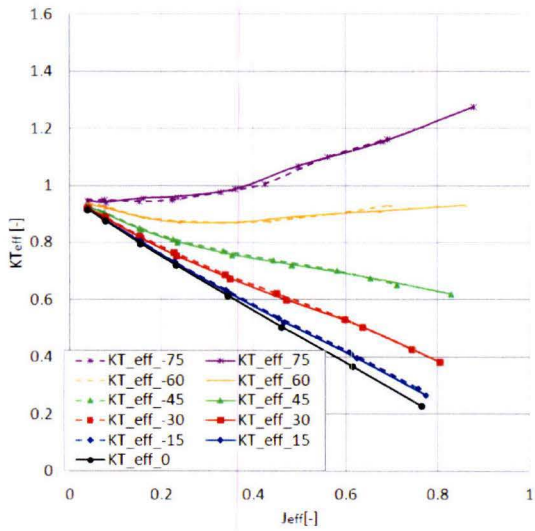

FIGURE 6.7: Thrust for various advance coefficients and heading angles, using modified coefficients.

heading angles. This behavior can still be found in the modified results. Therefore, this is not related to the relative change in angular velocity due to the disturbance of the thrusterhouse. The most obvious reason for this deviation behavior of the results for higher heading angles is the relation with the mass flow $\dot{m}$.

In Figure 6.10 and 6.11 it can be seen that the for low advance coeffients and heading angles the mass flow is for a large extent dependent of the rotation rate of the propeller, but for higher heading angles other phenomena are taken over. This phenomena will be discussed in more detail in section 6.3.1.

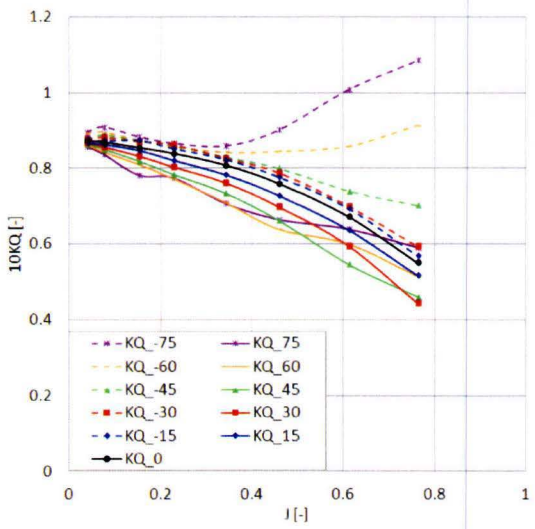

FIGURE 6.8: Torque for various advance coefficients and heading angles, using normal coefficients.

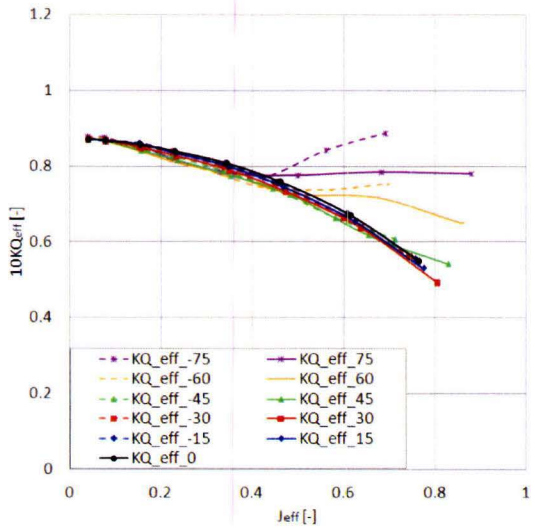

FIGURE 6.9: Torque for various advance coefficients and heading angles, using modified coefficients.

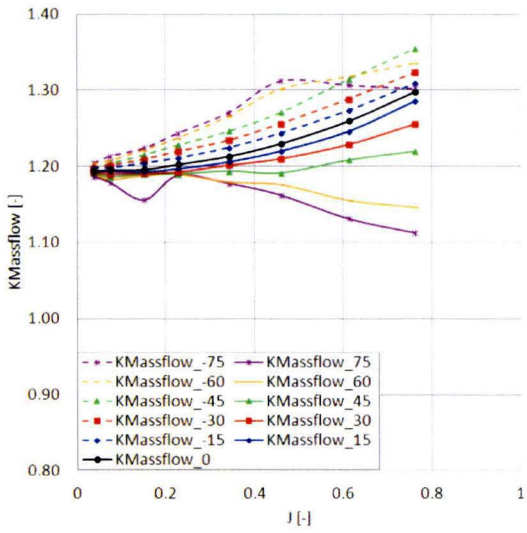

FIGURE 6.10: Mass flow for various advance coefficients and heading angles, using normal coefficients.

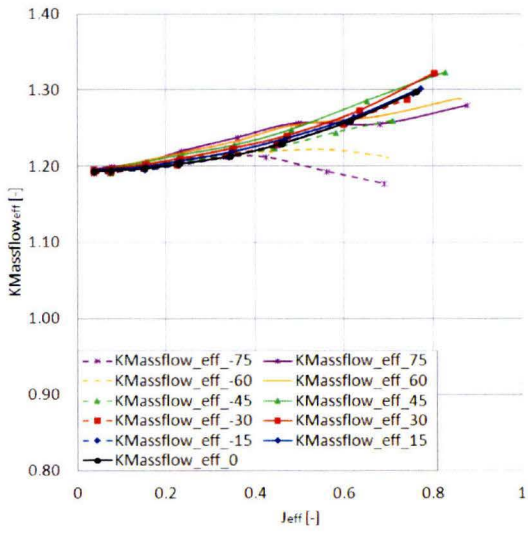

FIGURE 6.11: Mass flow for various advance coefficients and heading angles, using modified coefficients.

To determine this dimensionless term of the mass flow the following formulas are used:

$$\text{Mass flow coefficient} \quad K_{\dot{m}} = \frac{\dot{m}}{\rho n D^3} \tag{6.2}$$

$$\text{Effective mass flow coefficient} \quad K_{\dot{m}\,eff} = \frac{\dot{m}}{\rho n_{eff} D^3} \tag{6.3}$$

Because the side forces are pointing in opposite directions for negative and positive angles the corrected results for the negative heading angles are inverted in order to make a good comparison, see Figures 6.12 and 6.13. Especially for the lower advance coefficients the deviation between the negative and positive heading angles is reduced. It can be seen that for higher advance coefficients the deviation grows, between the negative and postive heading angles. The reason for the deviation to grow for higher advance coefficients is due to the fact that the side force is dominated by the velocity component in normal direction with respect to the propeller axis, and therefore not fully dependent on the angular velocity of the propeller. The effect of modifying the side force is not entirely correct for these conditions.

In Figure 6.14 and 6.15 the steering moment results are inverted as well, for a good comparison with the negative and positive heading angles. Again the results between the opposite angles show some nice results, especially at lower heading angles. At higher advance coefficients and heading angles, the flow phenomena around the thruster will change a lot. Therefore, differences occur for these operations conditions. Nevertheless, for substantial heading angles and advance coefficients, still in the range of good efficiency values, the occurring differences can be explained.

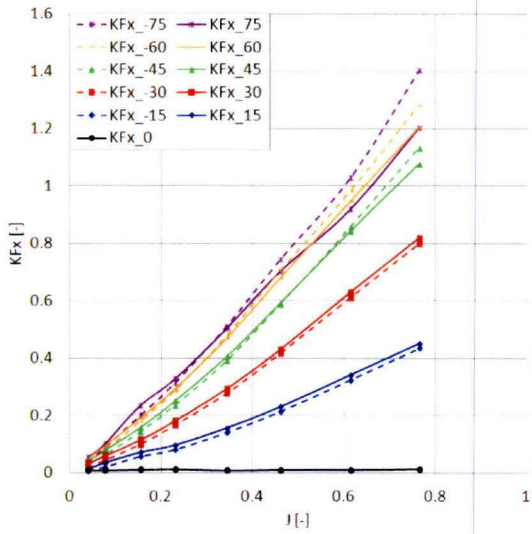

FIGURE 6.12: Side force for various advance coefficients and heading angles, using normal coefficients.

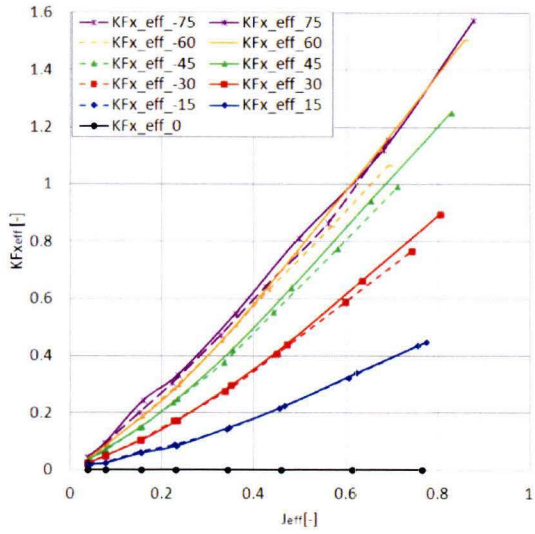

FIGURE 6.13: Side force for various advance coefficients and heading angles, using modified coefficients.

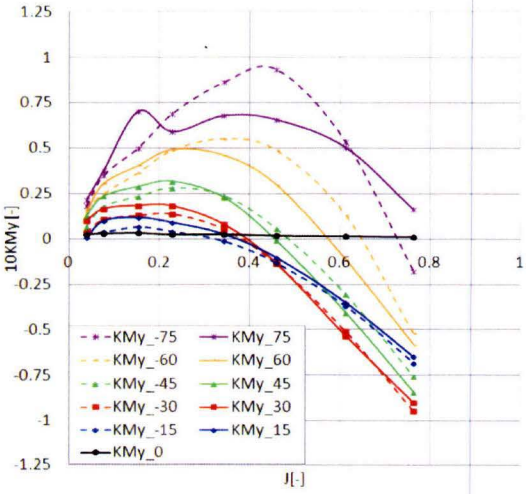

FIGURE 6.14: Steering moment for various advance coefficients and heading angles, using normal coefficients.

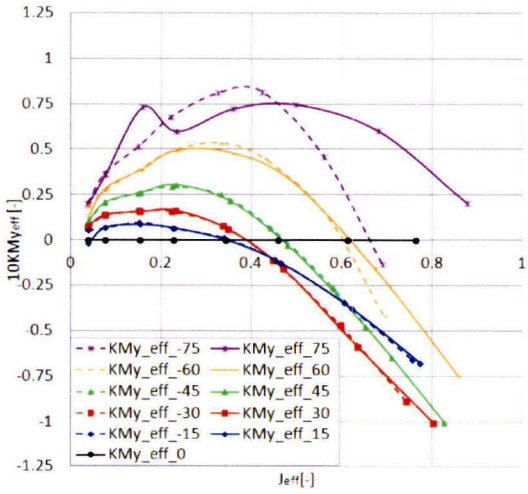

FIGURE 6.15: Steering moment for various advance coefficients and heading angles, using modified coefficients.

6.3.1 Rankine Half-Body Potential Flow

The flow passing the thruster could be seen as a potential flow of a uniform flow around a sink, a so-called a rankine half-body [13]. The flow field belonging to this problem, is strongly depending on two phenomena, the strength of the sink and the uniform flow. For low flow velocities the suction effect of the sink will dominate. Therefore, the incoming flow angles towards the sink does not lead to much changes in mass flow through the sink, because the flow is sucked into it, see Figure 6.16. When the incoming flow increases, this suction effect is not dominant anymore and the amount of flow passing the sink will increase, especcialy for higher heading angles. In Figure 6.17 stream lines are plotted for

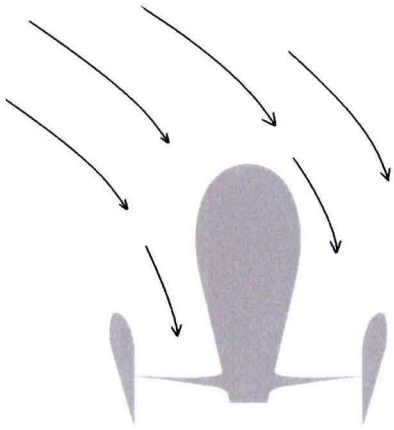

FIGURE 6.16: Rankine half-body potential flow.

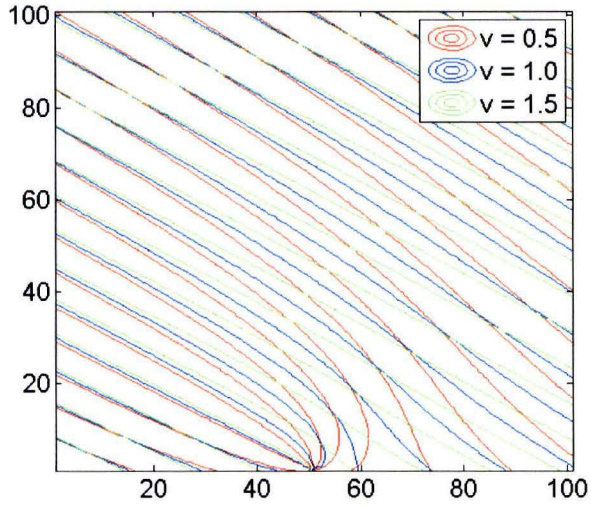

FIGURE 6.17: Rankine half-body potential flow.

various flow velocities for a heading angle of 60 degrees, to see the effect of the increase in velocity. It can be observed that the suction effect for the lowest inflow velocity causes a rather large deflection of the flow around the sink, while for higher inflow velocities this effect is a lot less. This results in less massflow through the sink.

6.3.2 Dependency of the Heading Angle

It is already mentioned that the side force components are also depending on the velocity components. It is therefore interesting to look at the velocity component acting in normal direction to the propeller axis, in stead of the advance speed V_a. This velocity component in the direction of the side force, is represented by the effective sideward coefficient $J_{x\,eff}$:

$$\text{Effective sideward coefficient} \quad J_{x\,eff} = \frac{V_a \sin(\delta)}{n_{eff} D} \tag{6.4}$$

For the side force it seems that this change of the velocity component, does not totally resolve the dependency of the heading angle, shown in Figure 6.18. The prediction of side forces is therefore not totally dependent of the velocity component. But for the side force moment the use of $J_{x\,eff}$ shows a remarkable result (Figure 6.19). It seems that the combination of side force and its arm, is almost fully dependent of the side velocity following from the heading angle.

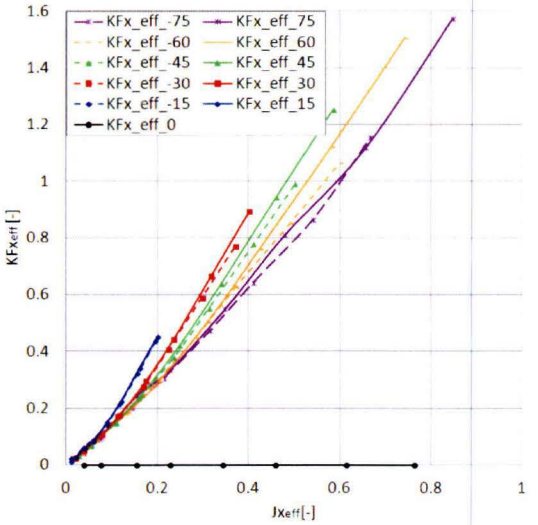

FIGURE 6.18: Side force for various side coefficients and heading angles, using modified coefficients.

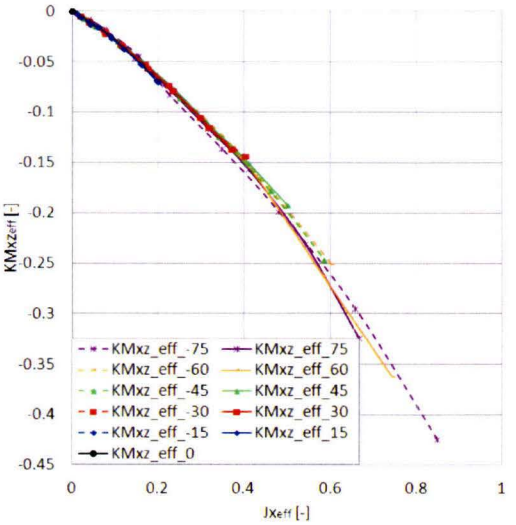

FIGURE 6.19: Side force moment for various side coefficients and heading angles, using modified coefficients.

Chapter 7

Dynamic Steering Behavior

In the previous chapters, a steerable thruster acting in oblique inflow for fixed heading angles with respect the incoming flow is reviewed. This configuration is for example used in one of the Heerema Marine Contractor semi-submersible crane vessels, the DCV Thialf [8]. But for steering purposes of the thruster unit, the position of the thruster is not fixed, so the heading angle will not be constant, but will vary in time. To see the difference between the fixed (quasi-steady) situation and the variable (dynamic) situation, numerical simulations are carried out to investigate the effect of the rotating behavior of the whole thruster unit. The possible differences are useful to get insight in the additional forces on the unit due to the dynamic steering motion of the thruster.

7.1 Experimental & Numerical Model Test Setup

For the dynamic steering action tests the same test setup is used as discussed in section 3.1. As for the oblique inflow tests, the thruster angle for the dynamic steering test, is governed by a PC-controlled servo. All the forces and moment are measured in the same way as the quasi-steady tests. For the analysis of the results, a low pass filter with a cut-off frequency of 8 Hz was applied to the measurements to remove noise. Although there is still some noise remaining on the presented signals, a lower filter frequency was avoided to not affect the rise time of forces, moments and thruster angle measurements too much.

For the setup of the dynamical model, the same computational domain can be used as for the static setup. To implement the rotating steering motion the boundary condition settings of the cylindrical domain needs to be changed to get the situation like Figure 7.1. A constant angular velocity is set to the cylindrical and the propeller domain to simulate the steering motion of the thruster unit around its steering axis. The remaining boundary setting are kept unchanged. This also holds for the timestep which is equivalent to a 2° propeller rotation. In general the rotation rate of the steering motion will be much lower than the propeller rotation. Therefore, the step size for the angular position will be much lower as well. In this case it will be equivalent to about 0.025°. As initial

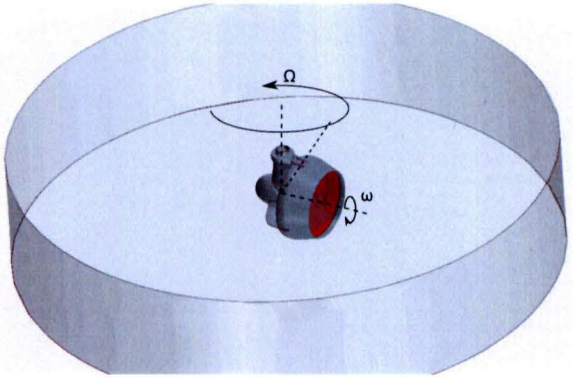

FIGURE 7.1: The angular velocities while steering.

condition the fully converged solution for the corresponding straight inflow conditions, so with the same propeller rotation rate and advance speed, is used.

7.2 Model Validation

As for the static validation, the numerical method has been validated with the aid of experimental data. These model scale measurements have been done in an open water set-up at Marintek in Norway. The dynamic steering action tests were performed for various steering rates Ω, so for different angular velocities of the thruster. One situation is taken to validate the numerical model for the dynamic steering action calculations. The thruster is validated for operation conditions v_a / n / J = 1.416m/s / 10.8 rps / 0.524 and supported with a steering rate Ω of 0.13 rps. Since the steering rate has a small start up and end time, there will not be a constant steering rate in the test conditions. For the numerical calculations a constant value steering rate is set, therefore a small difference will appear at the start and end of the steering action, see Figure 7.2. Taking this steering rate to be constant, the moments of inertia related to the moment of acceleration of the thruster, at the start and the end of the steering motion, are not taken into account in the numerical simulations.

The fully transient CFD results compared with the experimental results are shown in Figure 7.3. For these numerical simulations the method of moving mesh is used to simulate the motions. The fluctuations due to the propeller rotations are clearly visible in results. Since averaging the fluctuations is not straight forward in this case, because the results are not fluctuation around a constant value, the fluctuations are retained in the first instance. The comparison between the CFD results and the experimental data shows a good agreement over the whole range of heading angles. The same deviations in the steering moment K_{M_y} were found as for the static comparison with the experimental results. So, because the dynamic steering simulations shows the same trend as the static ones, it is assumed that the captured flow phenomena is acceptable.

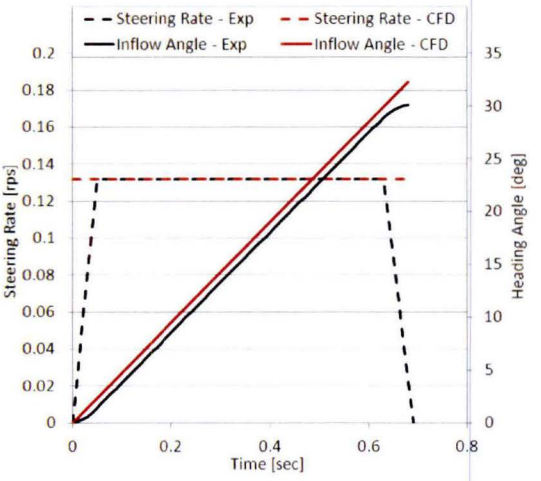

FIGURE 7.2: Steering rate and steering angle for the experiments and CFD.

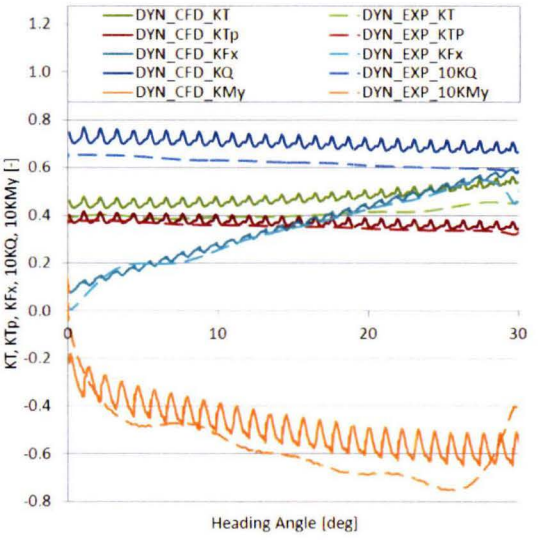

FIGURE 7.3: Comparison of the model scale experimental data with model scale CFD results.

7.3 Quasi-Steady versus Dynamic Steering Behavior

In Figure 7.4, the thrust and torque for the quasi-steady simulations are shown as dotted line and the dynamic results are shown as solid lines, for the condition v_a / n / Ω / J = 1.416 m/s / 10.8 rps / 0.13 rps / 0.524. For other operation conditions the results are shown in Appendix C. For the quasi-steady results the fluctuations caused by the propeller blades passing the thruster house were filtered by taking the averaged value of one propeller revolution. For the dynamic results these fluctuations are not filtered. Besides these fluctuations, no large deviations were found in the trend of the characteristics. Except for the side force, which shows a clear increase in value, it seems that this steering motion even with the relative small angular velocity adds a substantial amount of side force to the thruster unit. It is obvious that this increase in side force is transmitted to the hydrodynamic steering moment, showing an increase in absolute value.

Since the quasi-steady results were averaged the amplitudes for the varying heading angles was not visible. For the dynamic results, it can be seen that the fluctuations show a reasonable increase in amplitude, if the heading angle is gets above 30 degrees. For these conditions the orientation of the propeller blades does matter a lot, because the nozzle side will screen the propeller blade, which is temporarily positioned behind it. This leads to larger fluctuations in the performance results. Especially for the steering moment this amplitude takes relatively large values.

By making use of Fourier analyses, equation 7.1, it is possible to quantify a certain amplitude A_k and a certain phase shift ϕ_k of the results. The blade frequency is indicated

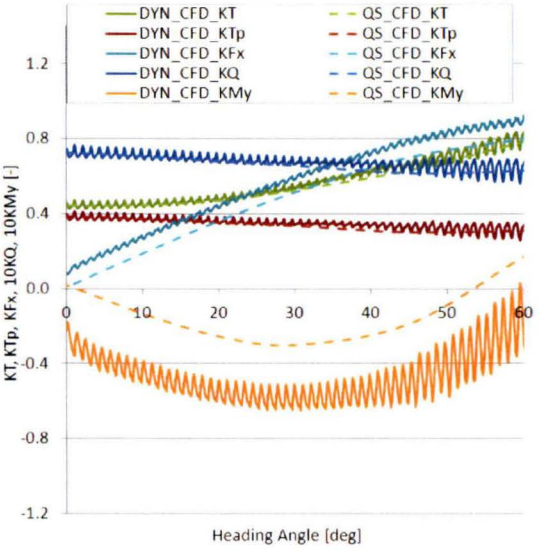

FIGURE 7.4: Comparison between the quasi-steady and dynamic CFD results.

with ω_0.

$$T(t,\delta) = A_0(\delta) + \sum_{k=1}^{\infty} A_k(\delta)\cos(k\omega_0 t + \phi_k(\delta)) \tag{7.1}$$

At first the increasing trend due to the steering motion should be subtracted from the results, leaving the fluctuations caused by the propeller blades, the blade harmonics. The steering and blade harmonics for the thrust component K_T are shown in Figure 7.5. The steering harmonic is obtained by a moving average of the results over one blade frequency, 90° for a four bladed propeller. On the remaining fluctuations a fourier analysis is applied, just for the first blade harmonic. These analysis are divided into two regions, lower steering angels from 0° to 20° and high steering angles from 50° to 60°.

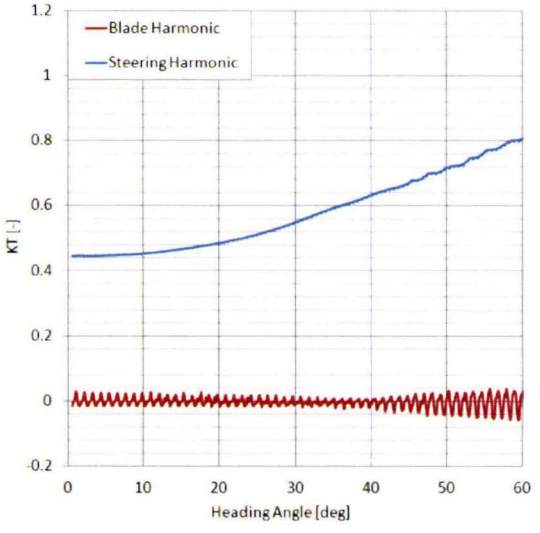

FIGURE 7.5: Steering and blade harmonics.

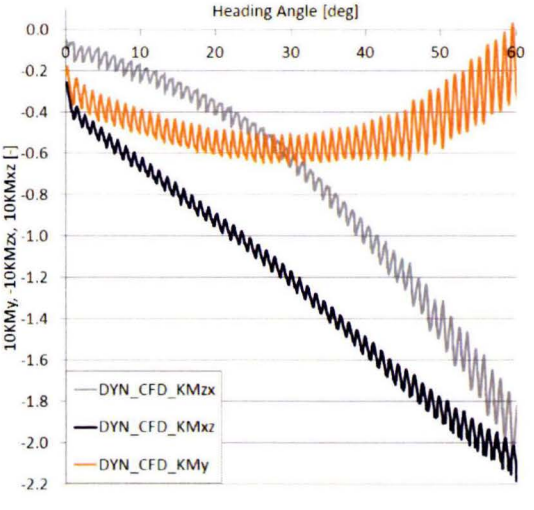

FIGURE 7.6: Anti-Phase of the thrust eccentricity moment and the side force moment.

The results of the analyses are listed in table 7.1. Observing the fluctuations, show that the amplitude of the characteristics increases to twice the size, or even more of the amplitude of lower steering angles, for higher steering angles. Looking at the phase differences of the components show that the two individual components of the hydrodynamic steering moment are more or less in anti-phase, see Figure 7.6. This causes that the total steering moment is relatively much more fluctuating than the other performance characteristics.

TABLE 7.1: Fourier Results.

δ	Mean amplitude A_k 0° - 20° (x10^{-3})	50° - 60°(x10^{-3})	Phase ϕ [deg]
K_T	14.6	46.3	172
K_{T_p}	14.8	40.7	160
K_{Fx}	10.0	20.3	155
$10K_Q$	22.2	57.4	160
$10K_{M_y}$	53.7	177.8	-17
$10K_{M_{xz}}$	27.8	63.0	138
$10K_{M_{zx}}$	31.5	126.0	-6

7.4 Dependency of the Steering Rates

The increase in the side force is dedicated to the increased relative velocity of the thruster unit with respect to the flow, resulting in an increase in drag force. For further analyses to quantify the behavior of this increase, several additional simulations are carried out. In Table 7.2 the different conditions are listed. These conditions are chosen in such a way that the behavior of changing the shaft speeds could be seen as well as the behavior of changing the steering rate.

TABLE 7.2: Different Dynamic Operation Conditions.

	1	2	3	4	5	6
V_a [m/s]	1.416	1.416	1.416	1.416	1.416	1.416
n [rps]	10.8	10.8	10.8	12	12	16
J [-]	0.52	0.52	0.52	0.47	0.47	0.35
Ω [rps]	0.09	0.13	0.2	0.13	0.2	0.13

In Figure 7.7 the side forces results are shown for different steering rates. Increasing the relative velocity by rotating the thruster unit, increases the side force. So for higher steering rates the forces will be higher than for lower rotation rates, at a constant propeller revolution rate.

For a good analysis of the side force for dynamic simulation and the difference with the quasi-steady results, the propeller harmonics needs to be filtered, so each condition will be represented by one single line, the steering harmonic. The determination of the steering harmonic is done using a moving average. Figure 7.8 and 7.9 show the averaged results, the quasi-steady results are illustrated as well to visualize the difference.

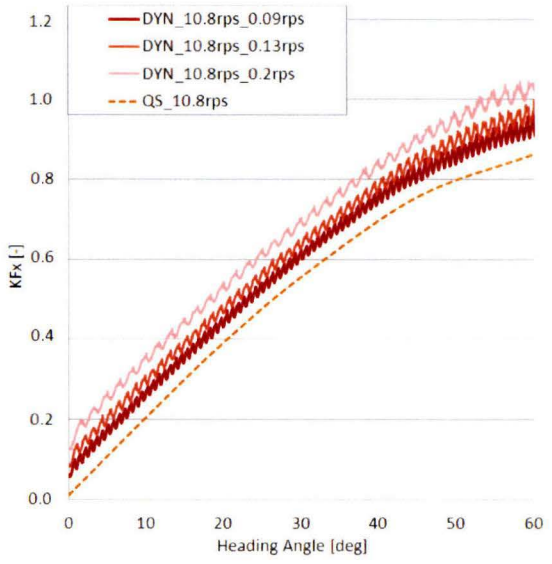

FIGURE 7.7: Side force for several dynamic conditions, varying Ω.

For the quasi-steady simulation the side force was only depending on the propeller rotation rate. It is obvious from the dynamic results that the behavior of the side force depends on both the propeller rotation rate and the steering motion. For now the focus will be on the additional side force dF_x, due to the dynamic steering action. dF_x could be determined by subtracting the quasi-steady results from the dynamic results:

$$dF_x = F_{xDyn} - F_{xQS} \tag{7.2}$$

In Figure 7.10 this is shown in non-dimensional form. Immediately, it can be seen that the shape of the additional side force is similar for all operation conditions. Because it was seen that the results are dependent of the propeller and the steering rotation rate, it was chosen to re-scale KdF_x. By using the following equation a re-scaled non-dimensionless term, KdF_{xDyn}, is formed for the the additional side force, due to the steering action.

$$\begin{aligned} KdF_{xDyn} &= \frac{dF_x}{\rho n^2 D^4} \cdot \frac{n}{\Omega} \\ &= \frac{dF_x}{\rho n \Omega D^4} \end{aligned} \tag{7.3}$$

The results of the additional side force, illustrated in Figure 7.11, are now independent of the steering rotation rate and the propeller rotation rate. It can be observed that the results show a good agreement with each other. Therefore is assumed that the size of the additional side force is fully referring to the combination of the operating steering rotation rate of the thruster unit and the propeller rotation rate, at least for a constant advance speed. While for quasi-steady results the side force is dependent of a combination between the propeller rotation rate and the magnitude of the inflow velocity. To verify this assumption the behavior of the drag forces of the thruster unit at various advance velocities and steering rates has to be studied. On top of that the influence of the shaft speed on these drag forces should be investigated. This falls out

of the scope of this thesis.

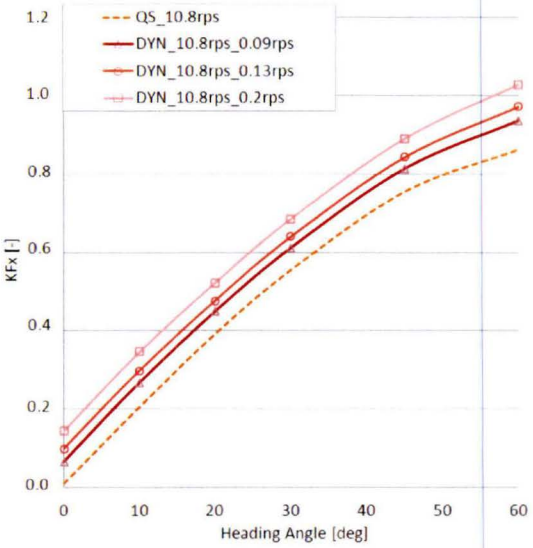

FIGURE 7.8: Averaged side force for several dynamic conditions, varying Ω.

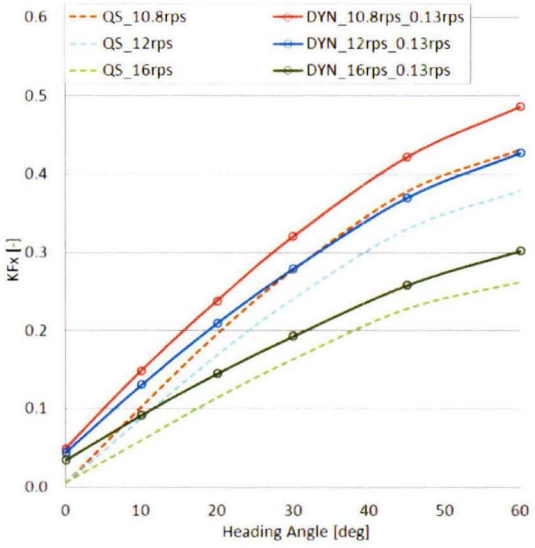

FIGURE 7.9: Averaged side force for several dynamic conditions, varying n, consequently J.

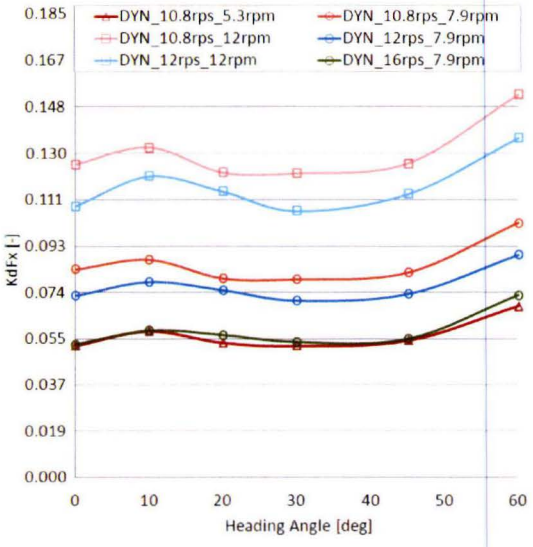

FIGURE 7.10: The additional side force due to the steering action.

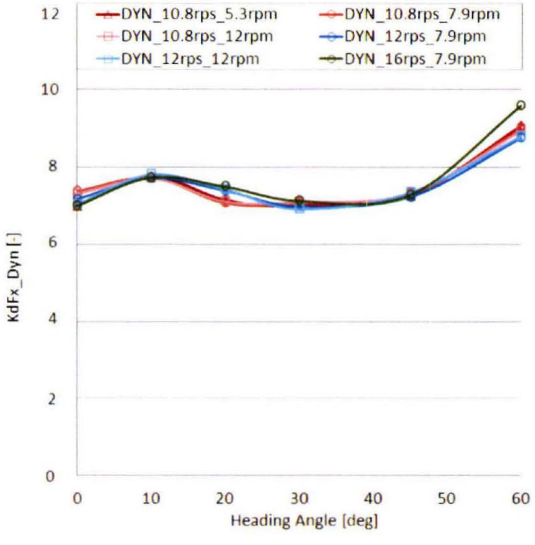

FIGURE 7.11: The re-scaled additional side force due to the steering action.

Chapter 8

Conclusions

For the mechanical design of the azimuth thrusters, including bearings, bevel gears and seals, it is important to identify the magnitudes of the forces and moments for oblique inflow conditions. The purpose of this thesis was to get insight in the behavior of the hydrodynamic loads on a steerable thruster.

For the hydrodynamic loads prediction a RANS-CFD method was used. The numerical estimations were compared with the model scale experimental data for several operating conditions and configurations. For all the validated cases, normal open water and oblique inflow conditions for fixed and moving inflow angles, the results provided reasonable agreement.

The transient hydrodynamic load predictions have been determined for many conditions, varying from inflow angles -90 degrees to 90 degrees over a whole range of ship speeds. The behavior of a steerable thruster operating at oblique inflow conditions is determined by the inflow velocity, rotation rate of the propeller and the steering angle of the unit. Numerical methods are also very wel suited to divide the thruster unit into different pieces, to see the contributions of the various parts of the thruster. It was found that the thrust forces could be related to both the propeller and the nozzle. While the side forces are mainly attributed to the nozzle.

In general the performance characteristics increase for large heading angles. Except for the hydrodynamic steering moment, which is a combination of both the thrust eccentricity of mainly the nozzle and the side force moment of mainly the nozzle as well. These counterbalancing components provide that the steering moment acts in both directions, depending on the heading angle of the thruster with respect to the flow and the ship speed. Besides the increasing performance characteristics for larger steering angles, an asymmetry in the results arise for negative and positive angles. It was found that the flow disturbance by the thruster house influences the flow field at the propeller plane in such a way that the performance changes in opposite way for negative and positive heading angles.

Comparison between the quasi-steady performance calculations and the performance calculations using the actual steering motion, highlighted an increase in side loads acting

on the thruster unit. This increase is caused by superposition of drag due to the rotation of the unit. Transmitting these increased side forces to the hydrodynamic steering moment causes an higher moment. The influence of the steering action does have a substantial effect on the hydrodynamic loads acting on the thruster unit.

Bibliography

[1] Amini, H. and S. Steen (2011, December). "experimental and theoretical analysis of propeller shaft loads in oblique inflow". *Journal of Ship Research, , Vol. 55*(nr. 4), pp. 268–288.

[2] Carlton, J. S. (2007). "marine propellers and propulsion". *Butterworth-Heinermann*, pp. 87–135.

[3] CD-adapco (2012). "star ccm user guide 7.04". *CD-adapco*.

[4] de Jager, A., M. Hoekstra, and N. Bulten (2004, September). "considerations on the application of the podded drive on dredgers". *9th PRADS Symposium, Lübeck / Travermünde*.

[5] Fox, R.W., M. A. (1985, June). "introduction to fluid mechanics". *John Wiley & Sons, New York ,Third Edition*.

[6] Glauert, H. (1935). "airplane propellers". *Durand WF (ed) Aerodynamic theory. Julius Springer, Berlin*.

[7] ITTC (2002). "model manufacture, ship models". *International Towing Tank Conference, Recommended Procedures and Guidelines - 7.5-02-03-01.1. Revision 01*.

[8] Ottens, H., N. Bulten, and R. van Dijk (2013, June). "full scale cfd validation on thruster-hull interaction on a semi-submersible crane vessel in transit condition.". *OMAE 2013-10350, Nantes, France*.

[9] Palm, M., D. Jürgens, and D. Bendl (2010, October 12-13). "comparison of thruster axis tilting versus nozzle tilting on the propeller-hull interactions for a drillship at dp-conditions". *Dynamic Positioning Conference*.

[10] Shih, T.-H., W. W. Liou, A. Shabbir, and J. Zhu (1995, March). "a new eddy-viscosity model for high reynolds number turbulent flows-medel development and validation.". *Comput. Fluids 24 (3)*, pp. 227–238.

[11] Srinivasa-Rao, P. (2010, January). "computational fluid dynamics". *InTech Europe*, pp. 286–306.

[12] van Dijk, T. and A. Aalbers (2001, September 18-19). ""what happens in water" the use of hydrodynamics to improve dp". *Dynamic Positioning Conference*.

[13] Veldman, A. and A. Velick (2007). "stromingsleer". *Rijksuniversiteit Groningen*, pp. 53–66.

[14] Versteeg, H.K., M. W. (1995). "an introduction to computational fluid dynamics". *Longman Scientific & Technical*.

Appendix A

Open Water Characteristic

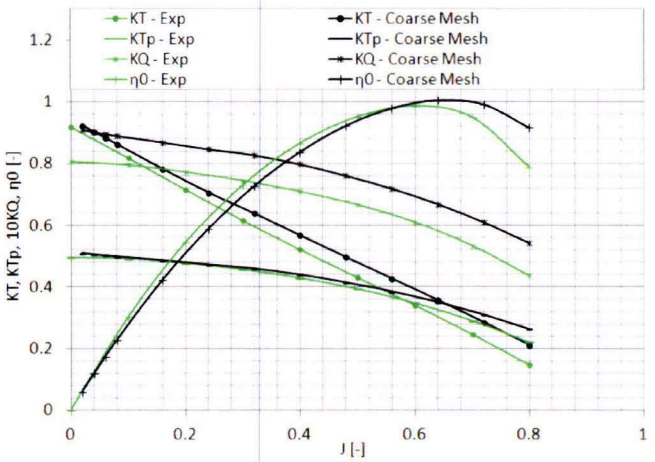

FIGURE A.1: Comparison model scale experimental data with model scale CFD results, coarse meshed, for thruster open water performance. (Propeller revolution of 16 rps)

Appendix B

Oblique Inflow Results, Numerical vs. Experimental

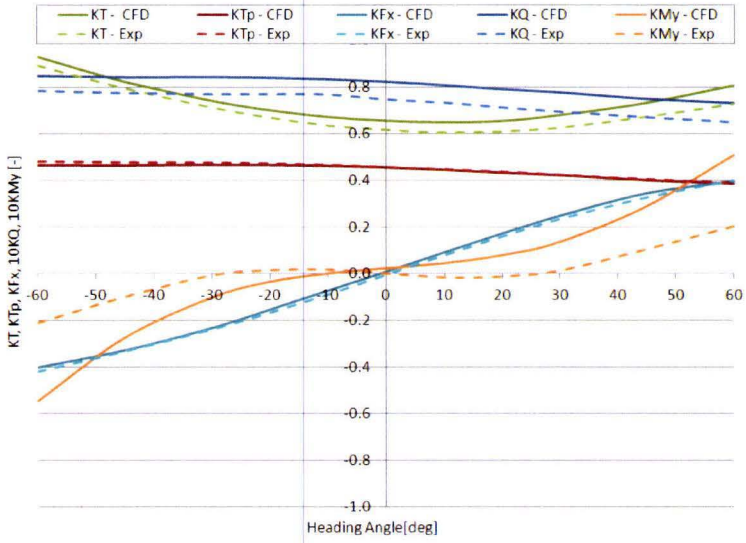

FIGURE B.1: Comparison model scale experimental data with model scale CFD results, coarse meshed, for thruster open water performance. (Propeller revolution of 12 rps and an advanced of 0.901 m/s)

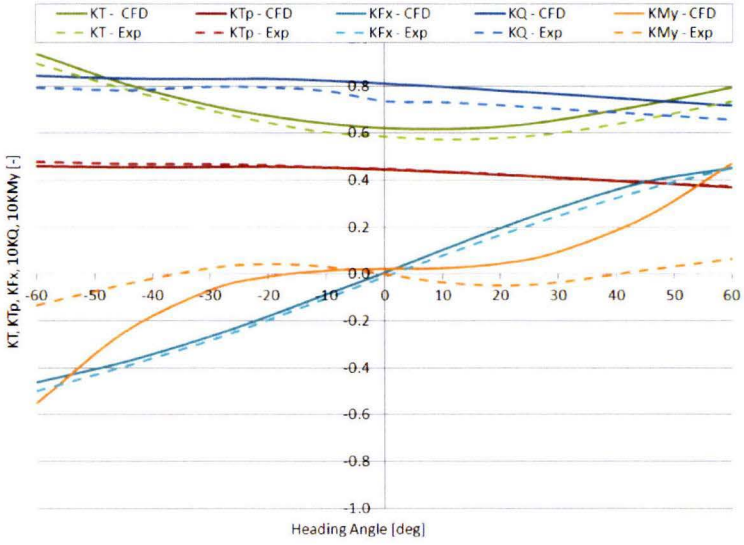

FIGURE B.2: Comparison model scale experimental data with model scale CFD results, coarse meshed, for thruster open water performance. (Propeller revolution of 10.8 rps and an advanced of 0.901 m/s)

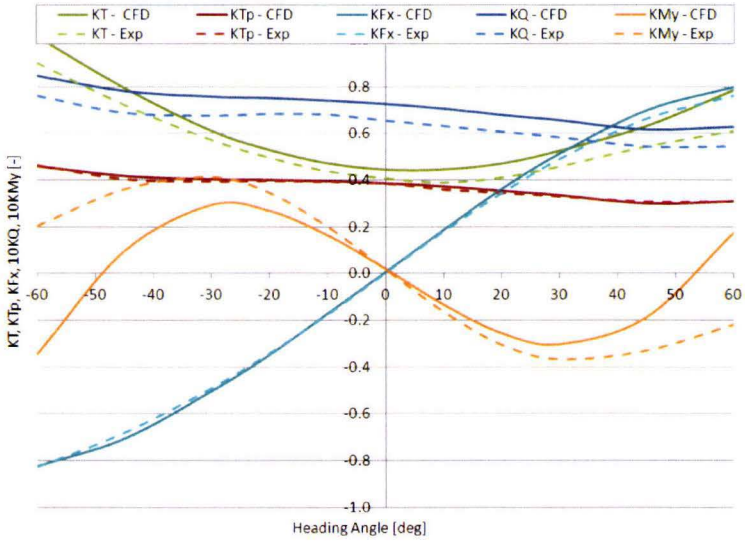

FIGURE B.3: Comparison model scale experimental data with model scale CFD results, coarse meshed, for thruster open water performance. (Propeller revolution of 10.8 rps and an advanced of 1.422 m/s)

Appendix C

Oblique Inflow Results, Dynamic vs. Quasi-Steady

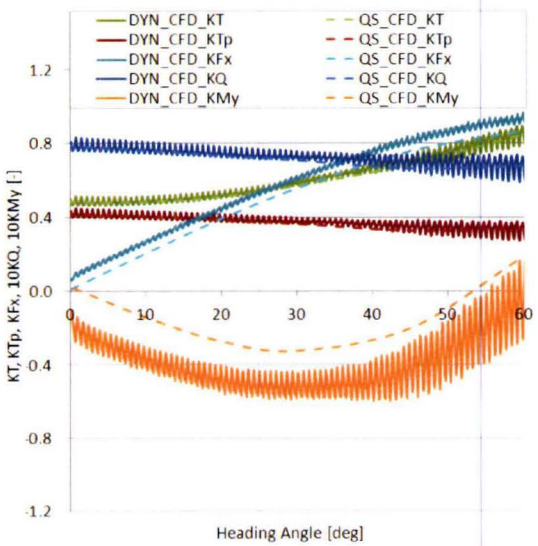

FIGURE C.1: Dynamic Results, v_a / n / Ω / J = 1.416m/s / 10.8 rps / 0.09 rps / 0.524

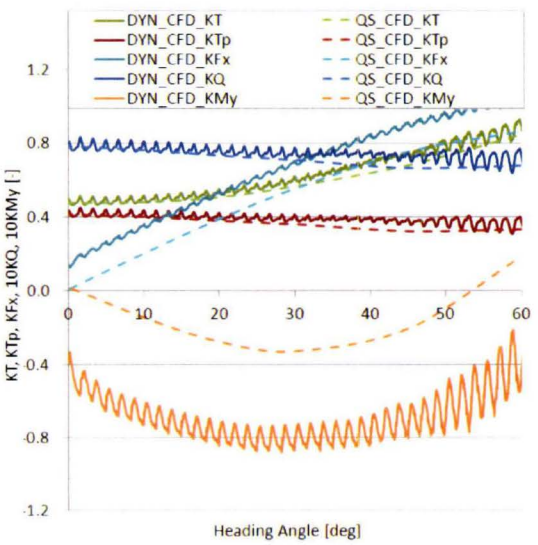

FIGURE C.2: Dynamic Results, v_a / n / Ω / J = 1.416m/s / 10.8 rps / 0.2 rps / 0.524

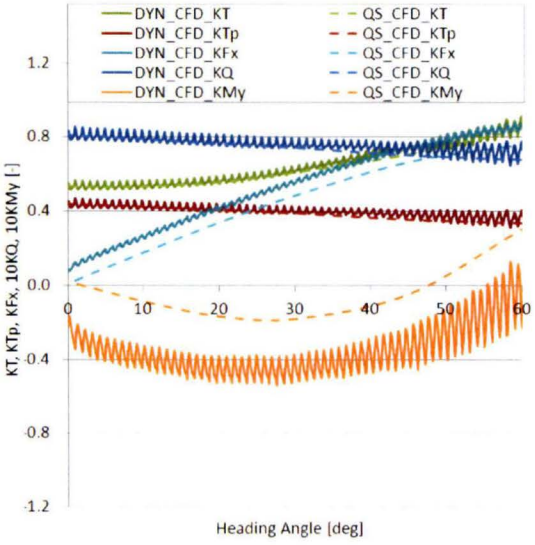

FIGURE C.3: Dynamic Results, v_a / n / Ω / J = 1.416m/s / 12 rps / 0.13 rps / 0.474

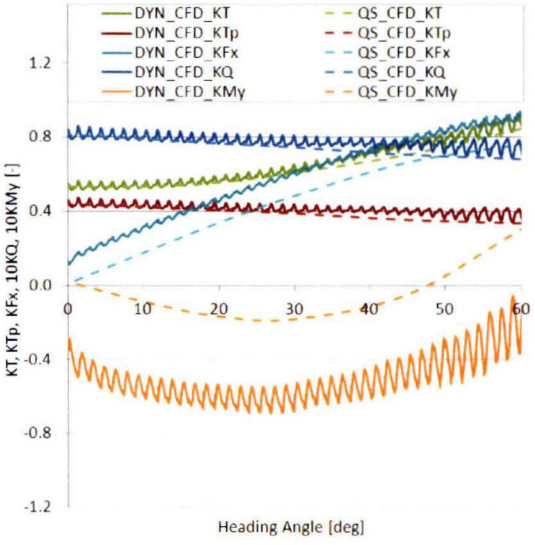

FIGURE C.4: Dynamic Results, v_a / n / Ω / J = 1.416m/s / 12 rps / 0.2 rps / 0.474

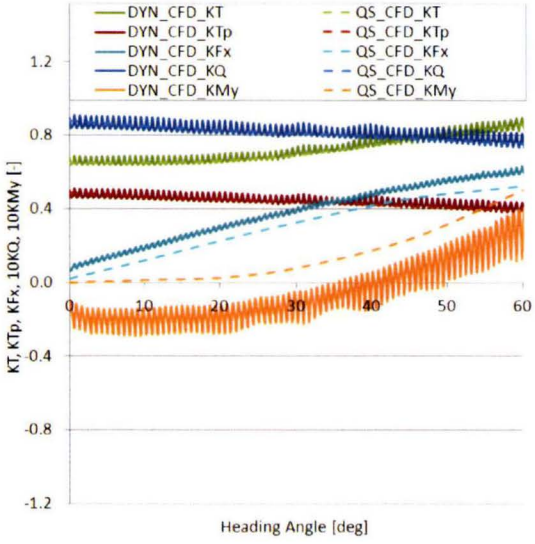

FIGURE C.5: Dynamic Results, v_a / n / Ω / J = 1.416m/s / 16 rps / 0.13 rps / 0.356